International Journal for Numerical Methods in Fluids

WILEY

RESEARCH ARTICLE OPEN ACCESS

A Non-Dissipative, Energy-Conserving, Arbitrary High-Order Numerical Method and Its Efficient Implementation for Incompressible Flow Simulation in Complex Geometries

Sreevatsa Anantharamu[1] | Krishnan Mahesh[1,2]

[1]Aerospace Engineering and Mechanics, University of Minnesota, Minneapolis, Minnesota, USA | [2]Naval Architecture and Marine Engineering, University of Michigan, Ann Arbor, Michigan, USA

Correspondence: Krishnan Mahesh (krmahesh@umich.edu)

Received: 30 October 2023 | **Revised:** 28 October 2024 | **Accepted:** 30 November 2024

Funding: This work was supported by the United States Office of Naval Research under grants N00014-21-1-2454.

Keywords: energy-conserving | high-order | hybridizable discontinuous Galerkin method | incompressible flows | non-dissipative

ABSTRACT

In the inviscid limit, the energy of a velocity field satisfying the incompressible Navier–Stokes equations is conserved. Non-dissipative numerical methods that discretely mimic this energy conservation feature have been demonstrated in the literature to be extremely valuable for robust and accurate large-eddy simulations of high Reynolds number incompressible turbulent flows. For complex geometries, such numerical methods have been traditionally developed using the finite volume framework and they have been at best second-order accurate. This paper proposes a non-dissipative and energy-conserving numerical method that is arbitrary high-order accurate for triangle/tetrahedral meshes along with its efficient implementation. The proposed method is a Hybridizable Discontinuous Galerkin (HDG) method. The crucial ingredients of the numerical method that lead to the discretely non-dissipative and energy-conserving features are: (i) The tangential velocity on the interior faces, just for the convective term, is set using the non-dissipative central scheme and the normal velocity is enforced to be continuous, that is, $H(\mathrm{div})$-conforming. (ii) An exactly (pointwise) divergence-free basis is used in each element of the mesh for the stability of the convective discretization. (iii) The combination of velocity, pressure, and velocity gradient spaces is carefully chosen to avoid using stabilization which would introduce numerical dissipation. The implementation description details our choice of the orthonormal and degree-ordered basis for each quantity and the efficient local and global problem solution using them. Numerical experiments demonstrating the various features of the proposed method are presented. The features of this HDG method make it ideal for high-order LES of incompressible flows in complex geometries.

1 | Introduction

Non-dissipative and discrete energy-conserving schemes are important for robust and accurate Large Eddy simulation (LES) of high-Reynolds number turbulent flows. By definition, in LES, the grid does not (or at best only partially) resolves the length scales at which turbulent dissipation occurs. Thus, the numerical accuracy of an LES can be very different between dissipative and non-dissipative schemes [1]. In LES with a non-dissipative scheme, the energy at length scales comparable to the mesh

size is controlled by the subgrid-model that provides a physically accurate dissipation rate. But, in LES with a dissipative scheme, the numerical dissipation can be quite large compared to the subgrid-scale dissipation for LES grids. Therefore, the large numerical dissipation controls the energy at scales comparable to the mesh size which can lead to underprediction of the energy at small scales. A problem with non-dissipative schemes is that they might be unstable for long-time integration, especially at high Reynolds numbers. The reason for this instability is that there is no inherent mechanism within the non-dissipative scheme to dampen the discretization errors and hence stabilize the kinetic energy (L^2-norm) of the solution. A way to ensure stability is to construct non-dissipative schemes such that the kinetic energy is discretely conserved in the inviscid limit. In this way, the energy of the solution remains bounded, and it ensures stability. But discrete kinetic energy is a derived quantity. Simply conserving the discrete momentum and mass does not always imply discrete kinetic energy conservation.

For complex geometries, non-dissipative and energy-conserving numerical methods have been traditionally developed using the finite volume framework and they have been at best second-order accurate. In this paper, we propose (i) a *non-dissipative, energy-conserving, arbitrary high-order* Hybridizable Discontinuous Galerkin (HDG) method to solve the incompressible Navier–Stokes equations for unstructured triangular/tetrahedral meshes, and (ii) its efficient implementation. To achieve both non-dissipativity and discrete energy conservation, we (i) carefully discretize the face velocity in the convective term using the central scheme only for the tangential component and a continuous face-normal component, (ii) use a pointwise (exactly) divergence-free polynomial space for the velocity in each element of the mesh for stability of the convective term, and (iii) carefully choose the element polynomial spaces of the different quantities approximated in each element to avoid using numerical stabilization for uniqueness. Details of an efficient implementation of the proposed method are also provided.

To discretely conserve the kinetic energy, the numerical scheme should satisfy the following conditions: (i) The convective discretization should satisfy a discrete chain rule identity which will cancel the contribution from the interior mesh entities to the energy contributed by the convective term. (ii) The discrete gradient matrix should be the transpose of the discrete divergence matrix. This transposition will cancel the contribution of the interior mesh entities to the energy contributed by the pressure-gradient term. For unstructured meshes, [2] and [3] constructed staggered finite-volume schemes that satisfy these conditions in two and three dimensions, respectively. These schemes satisfy condition (i) by discretizing the convective term in the rotational (Lamb) form. [4] constructed a collocated finite-volume scheme that incorporates a wide variety of mesh elements such as prisms, pyramids, tetrahedra, and hexahedra. Condition (i) is satisfied by this scheme by discretizing the convective term in the conservative form using a special scheme. The face-normal velocity in the convective flux is separately advanced in time such that it is discretely divergence-free. The cell velocity is interpolated to the faces using the central scheme, irrespective of the mesh. They further show that all collocated schemes satisfy condition (ii) only approximately. A new least-squares based pressure gradient reconstruction scheme was proposed that minimized this error in satisfaction of condition (ii). This method has been successfully applied for LES of flows in several complex geometries ranging from gas turbine combustors to marine propulsors. Several variants of this method have been developed, for example, [5], and [6]. For a review of discrete conservation properties of unstructured mesh schemes (mainly finite-volume), we refer the reader to [7]. We note that the above unstructured finite-volume schemes are at most second-order accurate. Extending them to be high-order within the finite-volume framework while satisfying conditions (i) and (ii) is very challenging and is still an open problem.

Another approach to construct high-order unstructured mesh schemes that obey conditions (i) and (ii) is via finite element methods [8]. Condition (ii) is automatically satisfied by finite element spaces that do not require pressure stabilization, such as the Taylor–Hood element, Scott–Vogelius element [9], and all mixed method spaces, for example, the Raviart–Thomas [10], Brezzi–Douglas–Marini [11] element, and the recent mixed method spaces of [12–14]. Enforcing condition (i) with finite element methods is tricky.

In finite elements where the divergence-free condition is imposed weakly but with a continuous velocity space (e.g., the Taylor–Hood element), the satisfaction of condition (i) depends only on the form of the convective term used for discretization. Discretizing the conservative ($\boldsymbol{\nabla}\cdot(\boldsymbol{u}\otimes\boldsymbol{u})$) and non-conservative ($\boldsymbol{u}\cdot(\boldsymbol{\nabla u})$) forms will not satisfy condition (i); we refer the reader to section 2 of [15] for a very informative discussion on this. But discretizing the skew-symmetric form [16], $\boldsymbol{\nabla}\cdot(\boldsymbol{u}\otimes\boldsymbol{u}))/2+(\boldsymbol{u}\cdot(\boldsymbol{\nabla u}))/2$, and the EMAC form [17], $\boldsymbol{u}\cdot(\boldsymbol{\nabla u}+\boldsymbol{\nabla u}^T)+\boldsymbol{u}\boldsymbol{\nabla}\cdot\boldsymbol{u}$, will satisfy condition (i). The skew-symmetric form, however, does not conserve momentum. The EMAC form conserves momentum but uses a modified pressure variable that relates to the kinematic pressure as $p-(\boldsymbol{u}\cdot\boldsymbol{u})/2$. This method has been extended to equal-order finite element spaces in [18] using pressure stabilization that adds some numerical dissipation. This method has been applied for LES over a full aircraft in [19]. Another modification of the non-linearity that satisfies condition (i) is outlined in [15]. Here, the weakly divergence-free velocity is postprocessed to be strongly divergence-free and used as the convective velocity in the convective term. We note that this postprocessing has some similarities to using a separate face-normal velocity in the finite-volume algorithm of [4]. Furthermore, if a discontinuous velocity space is used to weakly impose the divergence-free constraint, then in addition to the form of the convective term, the satisfaction of condition (i) also depends on the scheme used for the numerical convective flux. If the upwinding scheme is used, then the method will not satisfy condition (i) but if a central scheme is used, it will satisfy condition (i).

If the divergence-free constraint is imposed strongly (pointwise divergence-free) using a continuous velocity space, then condition (i) is automatically satisfied. Example is the Scott–Vogelius finite element [9] whose inf-sup stability is discussed in [20]. It has been applied to the Navier–Stokes equations in [21] and [22]. In [22], its results are compared to that of the EMAC scheme.

If a $H(div)$-conforming (continuous normal component of velocity across element boundaries but discontinuous tangential

component) velocity space is used to strongly impose the divergence-free constraint, then condition (i) is satisfied if a central scheme is used for the numerical convective flux on the interior faces [23]. used this for the incompressible Euler equations but their method converges suboptimally for odd polynomial degrees [24]. use a $H(\text{div})$-conforming velocity field for the incompressible Navier–Stokes equations, but they use an upwinding scheme for the numerical convective flux and, hence, do not satisfy condition (i). Our method produces a $H(\text{div})$-conforming velocity field for the incompressible Navier–Stokes equations and we use a central scheme and, thus, satisfy condition (i). Furthermore, numerical experiments show that our method shows optimal convergence for low and even very high Reynolds numbers.

The divergence-free condition on the velocities can be strongly imposed in multiple ways. One approach is to consider an appropriate combination of velocity and pressure spaces such that a weak imposition implies a strong imposition. This is the approach used in [25] and [21] for the incompressible Navier–Stokes equations and in [23] for the incompressible Euler equations. The other approach is hybridization. Here, a discontinuous velocity that is elementwise divergence-free is combined to be $H(\text{div})$-conforming via hybridization. One advantage of this approach is that the element pressure variable can be eliminated; only the average pressure in each element needs to be computed. This approach was used for the Stokes equation by the methods of [26, 27] and [28]. Recent HDG method of [29] uses this approach for the Stokes equation which was extended by [30] for the Brinkman equations. We use this approach for the incompressible Navier–Stokes equations. Furthermore, we present the implementation details of our efficient implementation. We use an orthonormal and degree-order basis functions for all the quantities. This simplifies certain aspects of the local and global problem solution.

The rest of the article is organized as follows. Section 2 discusses some background that the proposed hybridized discontinuous Galerkin method is based upon. Details of the method are described in Section 3 and a time-advancement algorithm is given in Section 4. Section 5 describes an efficient implementation using orthonormal basis functions. The proposed method is analyzed in Section 6, and in Section 7, we present numerical results demonstrating its various features. The article is summarized in Section 8.

2 | Background

2.1 | Navier–Stokes Equations: Velocity Gradient-Velocity-Pressure Formulation

The velocity gradient-velocity-pressure formulation of the Navier–Stokes equations is:

$$\boldsymbol{L} = \boldsymbol{\nabla u}, \qquad \text{in } \Omega \tag{1}$$

$$\frac{\partial \boldsymbol{u}}{\partial t} + \boldsymbol{\nabla}\cdot(\boldsymbol{u}\otimes\boldsymbol{u}) = -\boldsymbol{\nabla} p + \boldsymbol{\nabla}\cdot(\nu \boldsymbol{L}) + \boldsymbol{f}, \quad \text{in } \Omega, \text{ and} \tag{2}$$

$$\boldsymbol{\nabla}\cdot\boldsymbol{u} = 0, \qquad \text{in } \Omega \tag{3}$$

Here, Ω is the computational domain, $\boldsymbol{u}$ is the velocity, p is the pressure, $\boldsymbol{L}$ is the velocity gradient tensor, ν is the constant kinematic viscosity, and $\boldsymbol{f}$ is the body force. Density is absorbed in pressure. These equations are supplemented with the following boundary conditions on the domain boundary $\partial\Omega$. The domain boundary is split into periodic, Dirichlet, and outlet portions. On the periodic portion $\partial\Omega_P$, periodic boundary conditions are imposed (treated as an interior face). On the Dirichlet portion $\partial\Omega_D$, boundary conditions on the velocity, such as no-slip, slip/inflow boundary conditions, are imposed by setting $\boldsymbol{u} = \boldsymbol{u}_D$. On the outflow portion $\partial\Omega_O$, a freestream pressure is imposed by setting $(\nu\boldsymbol{L} - p\boldsymbol{I})\boldsymbol{n}$ equal to $-p_\infty \boldsymbol{n}$. Here, p_∞ is the freestream pressure and $\boldsymbol{I}$ is the identity tensor.

2.2 | A Characterization of the Exact Solution and Its Weak Form

We present a characterization of the above exact solution that is based on domain decomposition and also its weak form. Discretizing this weak form leads to the proposed method. Let the domain Ω be decomposed into a mesh of triangular elements in 2D or a mesh of tetrahedral elements in 3D. The exact solution is given by the Equations (1) to (3) can be equivalently characterized as follows. The quantities $\boldsymbol{L}$, $\boldsymbol{u}$, and p inside each element K of the mesh can be posed as a solution to the following problem:

$$\boldsymbol{L} = \boldsymbol{\nabla u}, \qquad \text{in } K \tag{4}$$

$$\frac{\partial \boldsymbol{u}}{\partial t} + \boldsymbol{\nabla}\cdot(\boldsymbol{u}\otimes\boldsymbol{u}) = -\boldsymbol{\nabla} p + \boldsymbol{\nabla}\cdot(\nu \boldsymbol{L}) + \boldsymbol{f}, \quad \text{in } K \tag{5}$$

$$\boldsymbol{\nabla}\cdot\boldsymbol{u} = 0, \qquad \text{in } K \tag{6}$$

$$\boldsymbol{u} = \hat{\boldsymbol{u}}, \qquad \text{on } \partial K, \text{ and} \tag{7}$$

$$\frac{1}{|K|}\int_K p \, d\Omega = \overline{p}_K, \tag{8}$$

where $\hat{\boldsymbol{u}}$ is the unknown velocity on the faces of the mesh and $\overline{p}_K$ is the unknown average pressure in each element K. $\hat{\boldsymbol{u}}$ and $\overline{p}_K$ are called hybrid variables. Equations for these hybrid variables are obtained by requiring the above $\boldsymbol{L}$, $\boldsymbol{u}$, and p in each element K to be identical to that of Equations (1) to (3). These equations turn out to be:

$$\left(\nu\boldsymbol{L}^+ - p^+\boldsymbol{I}\right)\boldsymbol{n}^+ + (\nu\boldsymbol{L}^- - p^-\boldsymbol{I})\boldsymbol{n}^- = 0, \text{on each interior face } F_i, \tag{9}$$

$$(\nu\boldsymbol{L} - p\boldsymbol{I})\boldsymbol{n} = -p_\infty\boldsymbol{n}, \text{ on each outlet boundary face } F_O, \tag{10}$$

$$\hat{\boldsymbol{u}} = \boldsymbol{u}_D, \text{ on each Dirichlet boundary face } F_D, \text{and} \tag{11}$$

$$\int_{\partial K} \hat{\boldsymbol{u}}\cdot\boldsymbol{n}\, d\Gamma = 0, \text{ for each element } K. \tag{12}$$

Here, $\boldsymbol{n}$ denotes the outward unit normal vector to an element, and superscripts + and − denote the value of the quantity in the two elements that neighbor the interior face. For the outlet boundary faces, the quantities $\boldsymbol{L}$ and p are that of the boundary element that contains the outlet boundary face. The first equation above imposes continuity of the normal component of the stress-like quantity $\nu\boldsymbol{L} - p\boldsymbol{I}$ across the interior faces. The second and third equations impose the outlet and Dirichlet boundary conditions, respectively. The fourth equation imposes the divergence-free constraint on $\hat{\boldsymbol{u}}$.

The above characterization of the exact solution can be posed in a weak form as follows. Multiplying Equation (4) with a test function $\boldsymbol{G} \in \left[C^0(K)\right]^{d\times d}$ and integrating by parts over element K yields

$$\int_K \boldsymbol{L}\cdot\boldsymbol{G}\mathrm{d}\Omega + \int_K \boldsymbol{u}\cdot(\boldsymbol{\nabla}\cdot\boldsymbol{G})\mathrm{d}\Omega = \sum_{F\in\partial K}\int_F \hat{\boldsymbol{u}}\cdot(\boldsymbol{G}\boldsymbol{n})\mathrm{d}\Gamma. \tag{13}$$

Note that on the boundary of element K, $\boldsymbol{u}$ is replaced with the hybrid variable $\hat{\boldsymbol{u}}$. Multiplying Equation (5) with a divergence-free test function $\boldsymbol{v} \in \{\left[C^0(K)\right]^d : \boldsymbol{\nabla}\cdot\boldsymbol{v} = 0\}$ and integrating by parts yields

$$\begin{aligned}\int_K \frac{\partial \boldsymbol{u}}{\partial t}\cdot\boldsymbol{v}\,\mathrm{d}\Omega - \int_K (\boldsymbol{u}\otimes\boldsymbol{u}):\boldsymbol{\nabla}\boldsymbol{v}\,\mathrm{d}\Omega + \sum_{F\in\partial K}\int_F \boldsymbol{f}_c(\hat{\boldsymbol{u}})\cdot\boldsymbol{v}\,\mathrm{d}\Gamma \\ = -\sum_{F\in\partial K}\int_F p\,\boldsymbol{v}\cdot\boldsymbol{n}\,\mathrm{d}\Gamma + \nu\int_K(\boldsymbol{\nabla}\cdot\boldsymbol{L})\cdot\boldsymbol{v}\,\mathrm{d}\Omega + \int_K \boldsymbol{f}\cdot\boldsymbol{v}\,\mathrm{d}\Omega,\end{aligned} \tag{14}$$

where the convective flux $\boldsymbol{f}_c(\hat{\boldsymbol{u}}) = (\hat{\boldsymbol{u}}\cdot\boldsymbol{n})\hat{\boldsymbol{u}}$. Note that the term $\int_K p\,\boldsymbol{\nabla}\cdot\boldsymbol{v}\,\mathrm{d}\Omega$ disappears because $\boldsymbol{\nabla}\cdot\boldsymbol{v} = 0$. Therefore, the pressure p appears above only in a face integral, and hence, needs to be defined only on the faces of the element. Finally, consider Equation (6). Multiplying it with a test function $q \in C^0(K)$, integrating by parts, replacing the $\boldsymbol{u}$ on the boundary by $\hat{\boldsymbol{u}}$, and integrating by parts again, we obtain

$$\sum_{F\in\partial K}\int_F \boldsymbol{u}\cdot\boldsymbol{n}\,q\,\mathrm{d}\Gamma = \sum_{F\in\partial K}\int_F \hat{\boldsymbol{u}}\cdot\boldsymbol{n}\,q\,\mathrm{d}\Gamma. \tag{15}$$

Observe that, similar to pressure p, the test function q also appears above only in face integrals. Hence, like pressure p, the test function q also needs to be defined only on the faces of the element. Consider Equation (8) where we impose the average pressure to be $\overline{p}_K$. Since the pressure is now defined only on the faces, this equation is replaced by the following equation:

$$\frac{1}{|\partial K|}\sum_{F\in\partial K}\int_F p\,\mathrm{d}\Gamma = \overline{p}_{\partial K},$$

where $\overline{p}_{\partial K}$ is the unknown average pressure on the faces of element K. Finally, consider the Equations (9) to (11). Multiplying them with a piecewise test function $\boldsymbol{\mu}\big|_F \in C^0(F)$ defined on each face F and integrating, we obtain

$$\int_{F_I}\left(\left(\nu\boldsymbol{L}^+ - p^+\boldsymbol{I}\right)\boldsymbol{n}^+ + \left(\nu\boldsymbol{L}^- - p^-\boldsymbol{I}\right)\boldsymbol{n}^-\right)\cdot\boldsymbol{\mu}\,\mathrm{d}\Gamma = 0, \tag{16}$$

for each interior face F_I,

$$\int_{F_N}((\nu\boldsymbol{L} - p\boldsymbol{I})\boldsymbol{n})\cdot\boldsymbol{\mu}\,\mathrm{d}\Gamma = -\int_{F_N} p_\infty\boldsymbol{\mu}\cdot\boldsymbol{n}\,\mathrm{d}\Gamma, \tag{17}$$

for each outlet boundary face F_O, and

$$\int_{F_D}\hat{\boldsymbol{u}}\cdot\boldsymbol{\mu}\,\mathrm{d}\Gamma = \int_{F_D}\boldsymbol{u}_D\cdot\boldsymbol{\mu}\,\mathrm{d}\Gamma, \tag{18}$$

for each Dirichlet boundary face F_D.

3 | Numerical Method

3.1 | Spatial Discretization

The spatial discretization of the proposed hyridized Discontinuous Galerkin method is obtained by performing the following replacements to the above weak form: (i) the exact solution $\boldsymbol{u}$, p, $\boldsymbol{L}$, $\hat{\boldsymbol{u}}$, and $\overline{p}_{\partial K}$ are replaced by the approximate solution $\boldsymbol{u}_h$, p_h, $\boldsymbol{L}_h$, $\hat{\boldsymbol{u}}_h$, and $\overline{p}_{h,\partial K}$, respectively, (ii) the convective flux $\boldsymbol{f}_c(\hat{\boldsymbol{u}})$ is replaced by the numerical convective flux $\boldsymbol{f}_{h,c}$, and (ii) finally, both the approximate solution and their corresponding test functions are required to belong to the following finite-dimensional subspaces: $\boldsymbol{u}_h$ and $\boldsymbol{v}$ belong to $\boldsymbol{V}_h(K)$, p and q belong to $P_h(\partial K)$, $\boldsymbol{L}_h$ and $\boldsymbol{G}$ belong to $\underline{\underline{\boldsymbol{W}}}_h(K)$, and $\hat{\boldsymbol{u}}_h$ and $\boldsymbol{\mu}$ belong to $\boldsymbol{M}_h$, where

$$\begin{aligned}\boldsymbol{V}_h(K) &= \text{set of functions } \boldsymbol{u}_h \in \left[P_k(K)\right]^d \text{ such that } \boldsymbol{\nabla}\cdot\boldsymbol{u}_h = 0,\\ P_h(\partial K) &= \text{set of functions } p_h \text{ defined piecewisely on each}\\ &\quad \text{face } F \text{ of element } K \text{ as } p_h\big|_F \in P_k(F),\\ \underline{\underline{\boldsymbol{W}}}_h(K) &= \text{set of } d\times d \text{ matrix-valued functions } \boldsymbol{L}_h \text{ such}\\ &\quad \text{that each of the } d \text{ rows of } \boldsymbol{L}_h \text{ belong to}\\ &\quad \text{the Raviart–Thomas space } \left[P_k(K)\right]^d \oplus \boldsymbol{x}\widetilde{P}_k(K), \text{ and}\\ \boldsymbol{M}_h &= \text{set of functions } \hat{\boldsymbol{u}}_h \text{ defined piecewisely on each face}\\ &\quad F \text{ of the mesh such that } \hat{\boldsymbol{u}}_h\big|_F \in \left[P_k(F)\right]^d,\\ &\quad \text{for all faces } F \text{ of the mesh.}\end{aligned}$$

The numerical convective flux $\boldsymbol{f}_{h,c}$ is defined as:

$$\boldsymbol{f}_{h,c} = (\hat{\boldsymbol{u}}_h\cdot\boldsymbol{n})(\hat{\boldsymbol{u}}_{h,T} + (\hat{\boldsymbol{u}}_h\cdot\boldsymbol{n})\boldsymbol{n}).$$

$\hat{\boldsymbol{u}}_{h,T}$ is the numerical tangential velocity on the faces of the mesh defined as

$$\hat{\boldsymbol{u}}_{h,T} = \frac{1}{2}\left(\boldsymbol{u}^+_{h,T} + \boldsymbol{u}^-_{h,T}\right), \qquad \text{for each interior face } F_i \tag{19}$$

$$\left.\begin{aligned}\hat{\boldsymbol{u}}_{h,T} &= \boldsymbol{u}_h - (\hat{\boldsymbol{u}}_h\cdot\boldsymbol{n})\boldsymbol{n}, \text{ if } \hat{\boldsymbol{u}}_h\cdot\boldsymbol{n} \geq 0,\\ \hat{\boldsymbol{u}}_{h,T} &= \hat{\boldsymbol{u}}_h - (\hat{\boldsymbol{u}}_h\cdot\boldsymbol{n})\boldsymbol{n}, \text{ if } \hat{\boldsymbol{u}}_h\cdot\boldsymbol{n} \leq 0,\end{aligned}\right\} \tag{20}$$

for each Dirichlet boundary face F_D, and

$$\hat{\boldsymbol{u}}_{h,T} = \hat{\boldsymbol{u}}_h - (\hat{\boldsymbol{u}}_h\cdot\boldsymbol{n})\boldsymbol{n}, \qquad \text{for each outlet boundary face } F_O. \tag{21}$$

On the interior faces, $\hat{\boldsymbol{u}}_{h,T}$ is set using the central scheme (first equation above). Here, $\boldsymbol{u}^+_{h,T} = \boldsymbol{u}^+_h - (\boldsymbol{u}^+_h\cdot\boldsymbol{n}^+)\boldsymbol{n}^+$ and $\boldsymbol{u}^-_{h,T} = \boldsymbol{u}^-_h - (\boldsymbol{u}^-_h\cdot\boldsymbol{n}^-)\boldsymbol{n}^-$. On the Dirichlet boundary faces, $\hat{\boldsymbol{u}}_{h,T}$ is set solely using the boundary data if the flow is entering the domain. If the flow is leaving the domain, then the $\hat{\boldsymbol{u}}_{h,T}$ on these faces is set using both the interior element velocity $\boldsymbol{u}_h$ and the face velocity $\hat{\boldsymbol{u}}_h$. This is necessary for a stable imposition of the Dirichlet boundary condition which is discussed more in Section 6.5. On the outlet boundary faces, $\hat{\boldsymbol{u}}_{h,T}$ is set using the face velocity $\hat{\boldsymbol{u}}_h$

This spatial discretization yields the following hybridized discontinuous Galerkin method for the semi-discrete solution (discretized in space, continuous in time). In each element K,

find the element velocity $\boldsymbol{u}_h$, element velocity gradient $\boldsymbol{L}_h$, and element pressure p_h belonging to the function spaces $\boldsymbol{V}_h(K)$, $\underline{\underline{\boldsymbol{W}_h}}(K)$, and $P_h(\partial K)$, respectively, such that

$$\int_K \boldsymbol{L}_h \cdot \boldsymbol{G}\mathrm{d}\Omega + \int_K \boldsymbol{u}_h \cdot (\boldsymbol{\nabla} \cdot \boldsymbol{G})\mathrm{d}\Omega = \sum_{F\in\partial K} \int_F \hat{\boldsymbol{u}}_h \cdot (\boldsymbol{G}\boldsymbol{n})\mathrm{d}\Gamma, \tag{22}$$

$$\begin{aligned} &\int_K \frac{\partial \boldsymbol{u}_h}{\partial t} \cdot \boldsymbol{v}\ \mathrm{d}\Omega - \int_K \left(\boldsymbol{u}_h \otimes \boldsymbol{u}_h\right) \cdot \boldsymbol{\nabla}\boldsymbol{v}\ \mathrm{d}\Omega \\ &+ \sum_{F\in\partial K} \int_F \boldsymbol{f}_{h,c}(\hat{\boldsymbol{u}}_h, \hat{\boldsymbol{u}}_{T,h}) \cdot \boldsymbol{v}_h\ \mathrm{d}\Gamma + \sum_{F\in\partial K} \int_F p_h\, \boldsymbol{v} \cdot \boldsymbol{n}\ \mathrm{d}\Gamma \\ &- \int_K \left(\boldsymbol{\nabla} \cdot \nu \boldsymbol{L}_h\right) \cdot \boldsymbol{v}\ \mathrm{d}\Omega = \int_K \boldsymbol{f} \cdot \boldsymbol{v}\ \mathrm{d}\Omega, \end{aligned} \tag{23}$$

$$\sum_{F\in\partial K} \int_F \boldsymbol{u}_h \cdot \boldsymbol{n}\ q\ \mathrm{d}\Gamma = \sum_{F\in\partial K} \int_F \hat{\boldsymbol{u}}_h \cdot \boldsymbol{n}\ q\ \mathrm{d}\Gamma, \text{ and} \tag{24}$$

$$\frac{1}{|\partial K|} \sum_{F\in\partial K} \int_F p_h\ \mathrm{d}\Gamma = \overline{p}_{h,\partial K}, \tag{25}$$

for all test functions $\boldsymbol{v}$, q, and $\boldsymbol{G}$ belonging to the function spaces $\boldsymbol{V}_h(K)$, $P_h(\partial K)$, and $\underline{\underline{\boldsymbol{W}_h}}(K)$, respectively. On each face F, find the face velocity $\hat{\boldsymbol{u}}_h$ and the separate tangential face velocity $\hat{\boldsymbol{u}}_{h,T}$ both belonging to the function space $\boldsymbol{M}_h$, and the average pressure $\overline{p}_{h,\partial K}$ in each element K, such that

$$\int_{F_I} \left(\left(\nu \boldsymbol{L}_h^+ - p_h^+ \boldsymbol{I}\right)\boldsymbol{n}^+ + \left(\nu \boldsymbol{L}_h^- - p_h^- \boldsymbol{I}\right)\boldsymbol{n}^-\right) \cdot \boldsymbol{\mu}\ \mathrm{d}\Gamma = 0, \tag{26}$$

for each interior face F_I,

$$\int_{F_N} \left(\left(\nu \boldsymbol{L}_h - p_h \boldsymbol{I}\right)\boldsymbol{n}\right) \cdot \boldsymbol{\mu}\ \mathrm{d}\Gamma = -\int_{F_N} p_\infty \boldsymbol{\mu} \cdot \boldsymbol{n}\ \mathrm{d}\Gamma, \tag{27}$$

for each outlet boundary face F_O,

$$\int_{F_D} \hat{\boldsymbol{u}}_h \cdot \boldsymbol{\mu}\ \mathrm{d}\Gamma = \int_{F_D} \boldsymbol{u}_D \cdot \boldsymbol{\mu}\ \mathrm{d}\Gamma, \tag{28}$$

for each Dirichlet boundary face F_D,

$$\sum_{F\in\partial K} \int_F \hat{\boldsymbol{u}}_h \cdot \boldsymbol{n}\ \mathrm{d}\Gamma = 0, \quad \text{for each element K}, \tag{29}$$

$$\hat{\boldsymbol{u}}_{h,T} = \frac{1}{2}\left(\boldsymbol{u}_{h,T}^+ + \boldsymbol{u}_{h,T}^-\right), \quad \text{for each interior face } F_I, \tag{30}$$

$$\left.\begin{aligned} \hat{\boldsymbol{u}}_{h,T} &= \boldsymbol{u}_h - (\hat{\boldsymbol{u}}_h \cdot \boldsymbol{n})\boldsymbol{n}, \text{ if } \hat{\boldsymbol{u}}_h \cdot \boldsymbol{n} \geq 0, \\ \hat{\boldsymbol{u}}_{h,T} &= \hat{\boldsymbol{u}}_h - (\hat{\boldsymbol{u}}_h \cdot \boldsymbol{n})\boldsymbol{n}, \text{ if } \hat{\boldsymbol{u}}_h \cdot \boldsymbol{n} \leq 0, \end{aligned}\right\} \tag{31}$$

for each Dirichlet boundary face F_D, and

$$\hat{\boldsymbol{u}}_{h,T} = \hat{\boldsymbol{u}}_h - (\hat{\boldsymbol{u}}_h \cdot \boldsymbol{n})\boldsymbol{n}, \quad \text{for each outlet boundary face } F_O, \tag{32}$$

for all test functions $\boldsymbol{\mu}$ belonging to the function space $\boldsymbol{M}_h$.

3.2 | Temporal Discretization

We time integrate the viscous, body force, and pressure terms using the implicit midpoint method, and the convective term using the Adams–Bashforth method. This time integration scheme is second-order accurate. Also, the storage in time is staggered. The velocity inside each element $\boldsymbol{u}_h$ is stored at time $t_n = n\Delta t$ while the velocity gradient $\boldsymbol{L}_h$, the face velocity $\hat{\boldsymbol{u}}_h$, and pressure p_h are stored at time $t_{n-1/2} = (n-1/2)\Delta t$. Here, Δt is the timestep. Combining the above spatial discretization with this temporal discretization leads to the following hybridized Discontinuous Galerkin method for the fully discrete solution.

3.3 | The Method

Let $\boldsymbol{u}_h^0$ and $\hat{\boldsymbol{u}}_h^0$ be the initial element and face velocity, respectively, at time $t = 0$. The procedure to prescribe them consistently using the exact initial velocity $\boldsymbol{u}(\boldsymbol{x}, t = 0)$ is given in Section 5.5. Let N be the total number of timesteps to be advanced and Δt be the timestep. For each time level $n = 1, \ldots, N$ do: In each element K, compute the element velocity $\boldsymbol{u}_h^n$, element velocity gradient $\boldsymbol{L}_h^{n-\frac{1}{2}}$, and element pressure $p_h^{n-\frac{1}{2}}$ belonging to the function spaces $\boldsymbol{V}_h(K)$, $P_h(\partial K)$, and $\underline{\underline{\boldsymbol{W}_h}}(K)$, respectively, such that

$$\int_K \boldsymbol{L}_h^{n-\frac{1}{2}} \cdot \boldsymbol{G}\mathrm{d}\Omega + \int_K \frac{\left(\boldsymbol{u}_h^n + \boldsymbol{u}_h^{n-1}\right)}{2} \cdot (\boldsymbol{\nabla} \cdot \boldsymbol{G})\mathrm{d}\Omega = \sum_{F\in\partial K} \int_F \hat{\boldsymbol{u}}_h^{n-\frac{1}{2}} \cdot (\boldsymbol{G}\boldsymbol{n})\mathrm{d}\Gamma, \tag{33}$$

$$\begin{aligned} &\int_K \frac{\boldsymbol{u}_h^n - \boldsymbol{u}_h^{n-1}}{\Delta t} \cdot \boldsymbol{v}\ \mathrm{d}\Omega - \int_K \left(\boldsymbol{\nabla} \cdot \nu \boldsymbol{L}_h^{n-\frac{1}{2}}\right) \cdot \boldsymbol{v}\ \mathrm{d}\Omega \\ &+ \sum_{F\in\partial K} \int_F p_h^{n-\frac{1}{2}}\, \boldsymbol{v} \cdot \boldsymbol{n}\ \mathrm{d}\Gamma \\ &= \int_K \left(\frac{3}{2}\boldsymbol{u}_h^{n-1} \otimes \boldsymbol{u}_h^{n-1} - \frac{1}{2}\boldsymbol{u}_h^{n-2} \otimes \boldsymbol{u}_h^{n-2}\right) \cdot \boldsymbol{\nabla}\boldsymbol{v}\ \mathrm{d}\Omega \\ &+ \sum_{F\in\partial K} \int_F \left(\frac{3}{2}\boldsymbol{f}_{h,c}(\hat{\boldsymbol{u}}_h^{n-1}, \hat{\boldsymbol{u}}_{T,h}^{n-1}) - \frac{1}{2}\boldsymbol{f}_{h,c}(\hat{\boldsymbol{u}}_h^{n-2}, \hat{\boldsymbol{u}}_{T,h}^{n-2})\right) \cdot \boldsymbol{v}\ \mathrm{d}\Gamma \\ &+ \int_K \boldsymbol{f}^{n-\frac{1}{2}} \cdot \boldsymbol{v}\ \mathrm{d}\Omega, \end{aligned} \tag{34}$$

$$\sum_{F\in\partial K} \int_F \frac{\left(\boldsymbol{u}_h^n + \boldsymbol{u}_h^{n-1}\right)}{2} \cdot \boldsymbol{n}\ q\ \mathrm{d}\Gamma = \sum_{F\in\partial K} \int_F \hat{\boldsymbol{u}}_h^{n-\frac{1}{2}} \cdot \boldsymbol{n}\ q\ \mathrm{d}\Gamma, \text{ and} \tag{35}$$

$$\frac{1}{|\partial K|} \sum_{F\in\partial K} \int_F p_h^{n-\frac{1}{2}}\ \mathrm{d}\Gamma = \overline{p}_{h,\partial K}^{n-\frac{1}{2}}, \tag{36}$$

for all test functions $\boldsymbol{v}$, q, and $\boldsymbol{G}$ belonging to the function spaces $\boldsymbol{V}_h(K)$, $P_h(\partial K)$, and $\underline{\underline{\boldsymbol{W}_h}}(K)$, respectively. Compute the face velocity $\hat{\boldsymbol{u}}_h^n$ belonging to the function space $\boldsymbol{M}_h$ and the average pressure $\overline{p}_{h,\partial K}^n$ in each element K, such that

$$\sum_{K\in\{K^+,K^-\}} \int_{F_I} \left(\nu \boldsymbol{L}_h^{n-\frac{1}{2}} - p_h^{n-\frac{1}{2}} \boldsymbol{I}\right)\boldsymbol{n} \cdot \boldsymbol{\mu}\ \mathrm{d}\Gamma = 0, \tag{37}$$

for each interior face F_I,

$$\int_{F_O} \left(\nu \boldsymbol{L}_h^{n-\frac{1}{2}} - p_h^{n-\frac{1}{2}} \boldsymbol{I}\right)\boldsymbol{n} \cdot \boldsymbol{\mu}\ \mathrm{d}\Gamma = -\int_{F_O} p_\infty \boldsymbol{\mu} \cdot \boldsymbol{n}\ \mathrm{d}\Gamma, \tag{38}$$

for each outlet boundary face F_O,

$$\int_{F_D} \hat{\boldsymbol{u}}_h^{n-\frac{1}{2}} \cdot \boldsymbol{\mu}\, \mathrm{d}\Gamma = \int_{F_D} \frac{\boldsymbol{u}_D^n + \boldsymbol{u}_D^{n-1}}{2} \cdot \boldsymbol{\mu}\, \mathrm{d}\Gamma, \tag{39}$$

for each Dirichlet boundary face F_D, and

$$\sum_{F\in\partial K} \int_F \hat{\boldsymbol{u}}_h^{n-\frac{1}{2}} \cdot \boldsymbol{n}\, \mathrm{d}\Gamma = 0, \qquad \text{for each element } K, \tag{40}$$

for all test functions $\boldsymbol{\mu}$ in the function space $\boldsymbol{M}_h$. Once $\boldsymbol{u}_h^n$ is obtained, update the numerical tangential face velocity $\hat{\boldsymbol{u}}_{h,T}^n$ as:

$$\hat{\boldsymbol{u}}_{h,T}^n = \frac{1}{2}\left(\boldsymbol{u}_{h,T}^{n^+} + \boldsymbol{u}_{h,T}^{n^-}\right), \qquad \text{for each interior face } F_I, \tag{41}$$

$$\left.\begin{aligned} \hat{\boldsymbol{u}}_{h,T}^n &= \boldsymbol{u}_h^n - (\hat{\boldsymbol{u}}_h^n \cdot \boldsymbol{n})\boldsymbol{n}, \text{ if } \hat{\boldsymbol{u}}_h^n \cdot \boldsymbol{n} \geq 0, \\ \hat{\boldsymbol{u}}_{h,T}^n &= \hat{\boldsymbol{u}}_h^n - (\hat{\boldsymbol{u}}_h^n \cdot \boldsymbol{n})\boldsymbol{n}, \text{ if } \hat{\boldsymbol{u}}_h^n \cdot \boldsymbol{n} \leq 0, \end{aligned}\right\} \tag{42}$$

for each Dirichlet boundary face F_D, and

$$\hat{\boldsymbol{u}}_{h,T}^n = \hat{\boldsymbol{u}}_h^n - (\hat{\boldsymbol{u}}_h^n \cdot \boldsymbol{n})\boldsymbol{n}, \text{ for each outlet boundary face } F_O. \tag{43}$$

where $\hat{\boldsymbol{u}}_h^n = 2\hat{\boldsymbol{u}}_h^{n-\frac{1}{2}} - \hat{\boldsymbol{u}}_h^{n-1}$. We note that the system of Equations (33) to (40) is an unsteady Stokes problem with the explicitly treated convective term absorbed into the body force. For the first timestep $n = 1$, the convective term is integrated using the backward Euler method by setting $\boldsymbol{u}_h^{-1}$, $\hat{\boldsymbol{u}}_h^{-1}$, and $\hat{\boldsymbol{u}}_{h,T}^{-1}$ to $\boldsymbol{u}_h^0$, $\hat{\boldsymbol{u}}_h^0$, and $\hat{\boldsymbol{u}}_{h,T}^0$, respectively.

4 | The Algorithm

As with all hybridized Discontinuous Galerkin methods, the elementwise quantities, $\boldsymbol{u}_h^n$, $\boldsymbol{L}_h^{n-\frac{1}{2}}$, and $p_h^{n-\frac{1}{2}}$, can be eliminated by constructing certain elementwise mappings. These mappings need to be constructed just once at the beginning of the simulation. It leads to a problem for only the face velocity $\hat{\boldsymbol{u}}_h^{n-\frac{1}{2}}$ and the average pressure $\overline{p}_{h,\partial K}^{n-\frac{1}{2}}$, and the resulting algorithm is described below.

Define $\boldsymbol{u}_h^{n-\frac{1}{2}} = (\boldsymbol{u}_h^n + \boldsymbol{u}_h^{n-1})/2$. In each element K, define the net body force $\boldsymbol{g}_h^{n-\frac{1}{2}}$ to be the function in $\boldsymbol{V}_h(K)$ that satisfies

$$\begin{aligned} \int_K \boldsymbol{g}_h^{n-\frac{1}{2}} \cdot \boldsymbol{v}\, \mathrm{d}\Omega &= \int_K \boldsymbol{f}^{n-\frac{1}{2}} \cdot \boldsymbol{v}\, \mathrm{d}\Omega \\ &+ \int_K \left(\frac{3}{2}\boldsymbol{u}_h^{n-1} \otimes \boldsymbol{u}_h^{n-1} - \frac{1}{2}\boldsymbol{u}_h^{n-2} \otimes \boldsymbol{u}_h^{n-2}\right) \cdot \boldsymbol{\nabla}\boldsymbol{v}\, \mathrm{d}\Omega \\ &- \sum_{F\in\partial K} \int_F \left(\frac{3}{2}\boldsymbol{f}_{h,c}(\hat{\boldsymbol{u}}_h^{n-1}, \hat{\boldsymbol{u}}_{T,h}^{n-1}) - \frac{1}{2}\boldsymbol{f}_{h,c}(\hat{\boldsymbol{u}}_h^{n-2}, \hat{\boldsymbol{u}}_{T,h}^{n-2})\right) \cdot \boldsymbol{v}\, \mathrm{d}\Gamma \\ &+ \frac{2}{\Delta t} \int_K \boldsymbol{u}_h^{n-1} \cdot \boldsymbol{v}\, d\Omega \end{aligned} \tag{44}$$

for all test functions $\boldsymbol{v}$ belonging to the function space $\boldsymbol{V}_h(K)$. Finally, define two elementwise mappings: $(\boldsymbol{u}_{\hat{\boldsymbol{u}}}(\boldsymbol{\mu}),\ \boldsymbol{L}_{\hat{\boldsymbol{u}}}(\boldsymbol{\mu}),\ p_{\hat{\boldsymbol{u}}}(\boldsymbol{\mu}))$, and $(\boldsymbol{u}_g(\boldsymbol{f}), \boldsymbol{L}_g(\boldsymbol{f}), p_g(\boldsymbol{f}))$. In each element K, $(\boldsymbol{u}_{\hat{\boldsymbol{u}}}(\boldsymbol{\mu}), \boldsymbol{L}_{\hat{\boldsymbol{u}}}(\boldsymbol{\mu}), p_{\hat{\boldsymbol{u}}}(\boldsymbol{\mu}))$ maps a piecewise function $\boldsymbol{\mu}$ belonging to $M_h(\partial K)$ to the functions $\boldsymbol{u}_{\hat{\boldsymbol{u}}}(\boldsymbol{\mu})$, $\boldsymbol{L}_{\hat{\boldsymbol{u}}}(\boldsymbol{\mu})$, and $p_{\hat{\boldsymbol{u}}}(\boldsymbol{\mu})$ belonging to the spaces $\boldsymbol{V}_h(K)$, $\underline{\underline{\boldsymbol{W}}}_h(K)$, and $\overline{P}_h(\partial K)$, respectively, such that

$$\begin{aligned} &\int_K \boldsymbol{L}_{\hat{\boldsymbol{u}}}(\boldsymbol{\mu}) \cdot \boldsymbol{G}\mathrm{d}\Omega + \int_K \boldsymbol{u}_{\hat{\boldsymbol{u}}}(\boldsymbol{\mu}) \cdot (\boldsymbol{\nabla} \cdot \boldsymbol{G})\mathrm{d}\Omega \\ &\quad = \sum_{F\in\partial K} \int_F \boldsymbol{\mu} \cdot (\boldsymbol{G}\boldsymbol{n})\mathrm{d}\Gamma, \end{aligned} \tag{45}$$

$$\begin{aligned} &-\nu \int_K \left(\boldsymbol{\nabla} \cdot \boldsymbol{L}_{\hat{\boldsymbol{u}}}(\boldsymbol{\mu})\right) \cdot \boldsymbol{v}\, \mathrm{d}\Omega + \frac{2}{\Delta t} \int_K \boldsymbol{u}_{\hat{\boldsymbol{u}}}(\boldsymbol{\mu}) \cdot \boldsymbol{v}\, \mathrm{d}\Omega \\ &+ \sum_{F\in\partial K} \int_F p_{\hat{\boldsymbol{u}}}(\boldsymbol{\mu})\, \boldsymbol{v} \cdot \boldsymbol{n}\, \mathrm{d}\Gamma = 0, \text{ and} \end{aligned} \tag{46}$$

$$\sum_{F\in\partial K} \int_F \boldsymbol{u}_{\hat{\boldsymbol{u}}}(\boldsymbol{\mu}) \cdot \boldsymbol{n}\, q\, \mathrm{d}\Gamma = \sum_{F\in\partial K} \int_F \boldsymbol{\mu} \cdot \boldsymbol{n}\, q\, \mathrm{d}\Gamma \tag{47}$$

for all test functions $\boldsymbol{v}$, $\boldsymbol{G}$, and q belonging to the function spaces $\boldsymbol{V}_h(K)$, $\underline{\underline{\boldsymbol{W}}}_h(K)$, and $\overline{P}_h(\partial K)$, respectively. Here, $M_h(\partial K)$ is the space of piecewise polynomials $\boldsymbol{\mu}$ defined on the boundary ∂K such that $\boldsymbol{\mu}|_F$ belongs to $[P_k(F)]^d$ for each F in ∂K. $\overline{P}_h(\partial K)$ is the subspace of $P_h(\partial K)$ consisting of only the zero-average functions, that is,

$$\overline{P}_h(\partial K) = \text{set of functions } q \text{ in } P_h(\partial K) \text{ that satisfy } \frac{1}{|K|} \sum_{F\in\partial K} \int_F q\, \mathrm{d}\Gamma = 0.$$

Further, in each element K, $(\boldsymbol{u}_g(\boldsymbol{f}), \boldsymbol{L}_g(\boldsymbol{f}), p_g(\boldsymbol{f}))$ maps a function $\boldsymbol{f}$ in $\boldsymbol{V}_h(K)$ to the functions $\boldsymbol{u}_g(\boldsymbol{f})$, $\boldsymbol{L}_g(\boldsymbol{f})$, and $p_g(\boldsymbol{f})$ belonging to the function spaces $\boldsymbol{V}_h(K)$, $\underline{\underline{\boldsymbol{W}}}_h(K)$, and $\overline{P}_h(\partial K)$, respectively, such that

$$\int_K \boldsymbol{L}_g(\boldsymbol{f}) \cdot \boldsymbol{G}_h\mathrm{d}\Omega + \int_K \boldsymbol{u}_g(\boldsymbol{f}) \cdot \left(\boldsymbol{\nabla} \cdot \boldsymbol{G}_h\right)\mathrm{d}\Omega = 0, \tag{48}$$

$$\begin{aligned} &-\nu \int_K \left(\boldsymbol{\nabla} \cdot \boldsymbol{L}_g(\boldsymbol{f})\right) \cdot \boldsymbol{v}_h\, \mathrm{d}\Omega + \frac{2}{\Delta t} \int_K \boldsymbol{u}_g(\boldsymbol{f}) \cdot \boldsymbol{v}_h\, \mathrm{d}\Omega \\ &+ \sum_{F\in\partial K} \int_F p_g(\boldsymbol{f})\, \boldsymbol{v}_h \cdot \boldsymbol{n}\, \mathrm{d}\Gamma = \int_K \boldsymbol{f} \cdot \boldsymbol{v}_h\, \mathrm{d}\Omega, \text{ and} \end{aligned} \tag{49}$$

$$\sum_{F\in\partial K} \int_F \boldsymbol{u}_g(\boldsymbol{f}) \cdot \boldsymbol{n}\, q_h\, \mathrm{d}\Gamma = 0 \tag{50}$$

for all test functions $\boldsymbol{v}$, $\boldsymbol{G}$, and q belonging to the function spaces $\boldsymbol{V}_h(K)$, $\underline{\underline{\boldsymbol{W}}}_h(K)$, and $\overline{P}_h(\partial K)$, respectively.

Using the definition of $\boldsymbol{u}_h^{n-\frac{1}{2}}$, the elementwise Equations (33) to (36) can be recast as a problem for $(\boldsymbol{u}_h^{n-\frac{1}{2}}, \boldsymbol{L}_h^{n-\frac{1}{2}}, p_h^{n-\frac{1}{2}})$. Further, using the above defined elementwise mappings, in each element K, this solution $(\boldsymbol{u}_h^{n-\frac{1}{2}}, \boldsymbol{L}_h^{n-\frac{1}{2}}, p_h^{n-\frac{1}{2}})$ can be decomposed as:

$$\begin{aligned} (\boldsymbol{u}_h^{n-\frac{1}{2}}, \boldsymbol{L}_h^{n-\frac{1}{2}}, p_h^{n-\frac{1}{2}}) &= \underbrace{(\boldsymbol{u}_{\hat{\boldsymbol{u}}}(\hat{\boldsymbol{u}}_h^{n-\frac{1}{2}}), \boldsymbol{L}_{\hat{\boldsymbol{u}}}(\hat{\boldsymbol{u}}_h^{n-\frac{1}{2}}), p_{\hat{\boldsymbol{u}}}(\hat{\boldsymbol{u}}_h^{n-\frac{1}{2}}))}_{\text{depends only on } \hat{\boldsymbol{u}}_h^{n-\frac{1}{2}} \text{ on } \partial K} \\ &+ \underbrace{(\boldsymbol{u}_g(\boldsymbol{g}_h^{n-\frac{1}{2}}), \boldsymbol{L}_g(\boldsymbol{g}_h^{n-\frac{1}{2}}), p_g(\boldsymbol{g}_h^{n-\frac{1}{2}}))}_{\text{depends only on } \boldsymbol{g}_h^{n-\frac{1}{2}}} \end{aligned}$$

$$+ \underbrace{(\mathbf{0}, \mathbf{0}, \overline{p}_{h,\partial K}^{n-\frac{1}{2}})}_{\text{depends only on } \overline{p}_{h,\partial K}^{n-\frac{1}{2}}} \tag{51}$$

Here, $(\boldsymbol{u}_{\hat{u}}(\hat{\boldsymbol{u}}_h^{n-\frac{1}{2}}), \boldsymbol{L}_{\hat{u}}(\hat{\boldsymbol{u}}_h^{n-\frac{1}{2}}), p_{\hat{u}}(\hat{\boldsymbol{u}}_h^{n-\frac{1}{2}}))$ is the solution to Equations (45) to (47) with $\boldsymbol{\mu} = \hat{\boldsymbol{u}}_h^{n-\frac{1}{2}}$. $(\boldsymbol{u}_g(\boldsymbol{g}_h^{n-\frac{1}{2}}), \boldsymbol{L}_g(\boldsymbol{g}_h^{n-\frac{1}{2}}), p_g(\boldsymbol{g}_h^{n-\frac{1}{2}}))$ is the solution to Equations (48) to (50) with $\boldsymbol{f} = \boldsymbol{g}_h^{n-\frac{1}{2}}$. $(\mathbf{0}, \mathbf{0}, \overline{p}_{h,\partial K}^{n-\frac{1}{2}})$ is the remaining portion which is just a constant pressure equal to $\overline{p}_{h,\partial K}^{n-\frac{1}{2}}$ and zero velocities. Substituting this decomposition in Equations (37) to (40) and manipulating yields the following problem just for the face velocity $\hat{\boldsymbol{u}}_h^{n-\frac{1}{2}}$ and the average pressure $\overline{p}_{h,\partial K}^{n-\frac{1}{2}}$. Find the face velocity $\hat{\boldsymbol{u}}_h^{n-\frac{1}{2}}$ belonging to the function space $\boldsymbol{M}_h$ and the average pressure $\overline{p}_{h,\partial K}^{n-\frac{1}{2}}$ in each element K, such that

$$\sum_{K\in\{K^+,K^-\}}\left[\int_K \nu \boldsymbol{L}_{\hat{u}}(\hat{\boldsymbol{u}}_h^{n-\frac{1}{2}}) \cdot \boldsymbol{L}_{\hat{u}}(\boldsymbol{\mu}_h^{(F_I)})\,\mathrm{d}\Omega + \frac{2}{\Delta t}\int_K \boldsymbol{u}_{\hat{u}}(\hat{\boldsymbol{u}}_h^{n-\frac{1}{2}}) \cdot \boldsymbol{u}_{\hat{u}}(\boldsymbol{\mu}_h^{(F_I)})\,\mathrm{d}\Omega\right] - \sum_{K\in\{K^+,K^-\}} \overline{p}_{h,\partial K}^{n-\frac{1}{2}} \int_{F_I} \boldsymbol{\mu}\cdot\boldsymbol{n}\,\mathrm{d}\Gamma = \sum_{K\in\{K^+,K^-\}}\int_K \boldsymbol{g}_h^{n-\frac{1}{2}} \cdot \boldsymbol{u}_{\hat{u}}(\boldsymbol{\mu}_h^{(F_I)})\,\mathrm{d}\Omega, \tag{52}$$

$$\int_K \nu \boldsymbol{L}_{\hat{u}}(\hat{\boldsymbol{u}}_h^{n-\frac{1}{2}}) \cdot \boldsymbol{L}_{\hat{u}}(\boldsymbol{\mu}_h^{(F_O)})\,\mathrm{d}\Omega + \frac{2}{\Delta t}\int_K \boldsymbol{u}_{\hat{u}}(\hat{\boldsymbol{u}}_h^{n-\frac{1}{2}}) \cdot \boldsymbol{u}_{\hat{u}}(\boldsymbol{\mu}_h^{(F_O)})\,\mathrm{d}\Omega - \overline{p}_{h,\partial K}^{n-\frac{1}{2}} \int_{F_O} \boldsymbol{\mu}\cdot\boldsymbol{n}\,\mathrm{d}\Gamma = -p_\infty \int_{F_O} \boldsymbol{\mu}\cdot\boldsymbol{n}\,\mathrm{d}\Gamma + \int_K \boldsymbol{g}_h^{n-\frac{1}{2}} \cdot \boldsymbol{u}_{\hat{u}}(\boldsymbol{\mu}_h^{(F_O)})\,\mathrm{d}\Omega - \tag{53}$$

$$\int_{F_D} \hat{\boldsymbol{u}}_h^{n-\frac{1}{2}} \cdot \boldsymbol{\mu}_h^{(F_D)}\,\mathrm{d}\Gamma = \int_{F_D} \frac{\boldsymbol{u}_D^n + \boldsymbol{u}_D^{n-1}}{2} \cdot \boldsymbol{\mu}_h^{(F_D)}\,\mathrm{d}\Gamma, \tag{54}$$

$$\sum_{F\in\partial K}\int_F \hat{\boldsymbol{u}}_h^{n-\frac{1}{2}} \cdot \boldsymbol{n}\,\mathrm{d}\Gamma = 0, \text{ for each element } K, \tag{55}$$

for all test functions $\hat{\boldsymbol{u}}_h^{(F_D)}$, $\hat{\boldsymbol{u}}_h^{(F_I)}$, and $\hat{\boldsymbol{u}}_h^{(F_O)}$ belonging to the function space $\boldsymbol{M}_h^{(F_D)}$, $\boldsymbol{M}_h^{(F_I)}$, and $\boldsymbol{M}_h^{(F_O)}$, respectively. Here, $\boldsymbol{M}_h^{(F_D)}$, $\boldsymbol{M}_h^{(F_I)}$, and $\boldsymbol{M}_h^{(F_O)}$ are the subspaces of $\boldsymbol{M}_h$ comprising of functions that are non-zero only on the Dirichlet boundary, interior, and outlet boundary faces, respectively. In hybridized Discontinuous Galerkin terminology, the above equations for $\hat{\boldsymbol{u}}_h^{n-\frac{1}{2}}$ and $p_{h,\partial K}^{n-\frac{1}{2}}$ are referred to as the "global problem". And, the equations for the two elementwise linear mappings (Equations (45) to (47) and (48) to (50)) are referred to as the "local problem".

The above elimination of the elementwise variables leads to the following time-advancement algorithm:

- In each element K, compute the elementwise linear mappings $(\boldsymbol{u}_{\hat{u}}(\boldsymbol{\mu}), \boldsymbol{L}_{\hat{u}}(\boldsymbol{\mu}), p_{\hat{u}}(\boldsymbol{\mu}))$ and $(\boldsymbol{u}_g(\boldsymbol{f}), \boldsymbol{L}_g(\boldsymbol{f}), p_g(\boldsymbol{f}))$ defined by Equations (45) to (47) and (48) to (50), respectively.
- Compute $\boldsymbol{u}_h^0$ and $\hat{\boldsymbol{u}}_h^0$ by projecting the initial data $\boldsymbol{u}(\boldsymbol{x}, t=0)$ as described in Section 5.5.
- Compute $\boldsymbol{u}_{h,T}^0$ from $\boldsymbol{u}_h^0$ and $\hat{\boldsymbol{u}}_h^0$ using Equations (41) to (43).
- For each time level $n = 1, \ldots, N$, do:
  - In each element K, compute the net body force $\boldsymbol{g}_h^{n-\frac{1}{2}}$ using Equation (44).
  - Compute the face velocity $\hat{\boldsymbol{u}}_h^{n-\frac{1}{2}}$ and the average pressure $\overline{p}_{h,\partial K}^{n-\frac{1}{2}}$ in each element K using Equations (52) to (55).
  - In each element K, compute the element velocity $\boldsymbol{u}_h^{n-\frac{1}{2}}$, velocity gradient $\boldsymbol{L}_h^{n-\frac{1}{2}}$, and pressure $p_h^{n-\frac{1}{2}}$ using Equation (51).
  - Update $\boldsymbol{u}_h^n$ and $\hat{\boldsymbol{u}}_h^n$ as $\boldsymbol{u}_h^n = 2\boldsymbol{u}_h^{n-\frac{1}{2}} - \boldsymbol{u}_h^{n-1}$ and $\hat{\boldsymbol{u}}_h^n = 2\hat{\boldsymbol{u}}_h^{n-\frac{1}{2}} - \hat{\boldsymbol{u}}_h^{n-1}$, respectively.
  - Compute $\boldsymbol{u}_{h,T}^n$ from $\boldsymbol{u}_h^n$ and $\hat{\boldsymbol{u}}_h^n$ using Equations (41) to (43).

5 | Algorithm Implementation

5.1 | Basis Functions

We note that irrespective of the choice of the basis functions, the computed numerical solution will be the same. This is because the numerical solution is determined by the function spaces, not by the choice of the basis functions for the function spaces. We present our choice of the basis functions below. Our basis functions are orthonormal. With this choice, the mass matrices will become diagonal matrices.

5.1.1 | Element Velocity

In each element K, the divergence-free space $\boldsymbol{V}_h(K)$ is used for the element velocity $\boldsymbol{u}_h$. Recall, $\boldsymbol{V}_h(K)$ is the set of functions in $\left[P_k(K)\right]^d$ that are exactly divergence-free. We use the efficient methodology of [31] to construct an orthonormal basis for this divergence-free polynomial subspace. We denote the obtained basis as $\boldsymbol{\varphi}_1^{(K)}, \ldots, \boldsymbol{\varphi}_{n_u}^{(K)}$, where $n_u = dC_d^{k+d} - C_d^{k-1+d}$ is the number of basis functions in each element. These functions satisfy the orthonormality condition $\int_K \boldsymbol{\varphi}_i^{(K)} \cdot \boldsymbol{\varphi}_j^{(K)}\,\mathrm{d}\Omega = \delta_{ij}|K|$ and, of course, the divergence-free condition $\boldsymbol{\nabla}\cdot\boldsymbol{\varphi}_i = 0$. The approximate velocity $\boldsymbol{u}_h(\boldsymbol{x}, t)$ in element K is expanded using this basis as:

$$\boldsymbol{u}_h(\boldsymbol{x}, t) = \sum_{i=1}^{n_u} \mathrm{u}_\mathrm{i}^{(\mathrm{K})}(t)\boldsymbol{\varphi}_i^{(K)}(\boldsymbol{x}),$$

where, $\mathrm{u}_1^{(K)}(t), \ldots, \mathrm{u}_{n_u}^{(K)}(t)$ are the degrees of freedom that only depend on time t. They relate to $\boldsymbol{u}_h$ as:

$$\mathrm{u}_\mathrm{i}^{(K)}(t) = \frac{1}{|K|}\int_K \boldsymbol{u}_h(\boldsymbol{x}, t) \cdot \boldsymbol{\varphi}_i^{(K)}\,\mathrm{d}\Omega;\ i = 1, \ldots, n_u.$$

5.1.2 | Element Velocity Gradient

For the velocity gradient $\boldsymbol{L}_h$ in each element K, we use the function space $\underline{\underline{\boldsymbol{W}}}_h(K)$. Recall, $\underline{\underline{\boldsymbol{W}}}_h(K)$ is the set of function in $[P_{k+1}(K)]^{d\times d}$ whose each row belongs to the Raviart–Thomas space, $\left[P_k(K)\right]^d \oplus \boldsymbol{x}\widetilde{P}_k(K)$. We use the orthonormal basis $\boldsymbol{\Phi}_1^{(K)}, \ldots, \boldsymbol{\Phi}_{n_L}^{(K)}$ for this space, where $n_L = d(dC_d^{k+d} + C_{d-1}^{k+d-1})$ is the number of basis functions in each element. They are defined as $\boldsymbol{\Phi}_{(i-1)n_{RT}+j}^{(K)} = \boldsymbol{e}_i \otimes \boldsymbol{\eta}_j^{(K)} = \boldsymbol{e}_i\left[\boldsymbol{\eta}_j^{(K)}\right]^T$, where $i = 1, \ldots, d; j = 1, \ldots, n_{RT}$, and $\boldsymbol{\eta}_1^{(K)}, \ldots, \boldsymbol{\eta}_{n_{RT}}^{(K)}$ is an orthonormal

basis for the Raviart–Thomas space. $n_{RT} = dC_d^{k+d} + C_{d-1}^{k+d-1}$ is the dimension of this space. These functions $\boldsymbol{\eta}_i^{(K)}$ satisfy the orthonormality relation, $\int_K \boldsymbol{\eta}_i^{(K)} \cdot \boldsymbol{\eta}_j^{(K)} \, \mathrm{d}\Omega = \delta_{ij}|K|$. Hence, the basis functions $\boldsymbol{\Phi}_1^{(K)}, \ldots, \boldsymbol{\Phi}_{n_L}^{(K)}$ are also orthonormal to each other satisfying the relation: $\int_K \boldsymbol{\Phi}_i^{(K)} \cdot \boldsymbol{\Phi}_j^{(K)} \, \mathrm{d}\Omega = \delta_{ij}|K|$. In each element K, the velocity gradient is expanded as

$$\boldsymbol{L}_h(\boldsymbol{x}, t) = \sum_{i=1}^{n_L} \mathrm{L}_{\mathrm{i}}^{(\mathrm{K})}(t) \boldsymbol{\Phi}_i^{(K)}(\boldsymbol{x}),$$

where $\mathrm{L}_{\mathrm{i}}^{(K)}(t)$ are the degrees of freedom that depend only on time t. They relate to $\boldsymbol{L}_h$ as:

$$\mathrm{L}_{\mathrm{i}}^{(K)}(t) = \frac{1}{|K|} \int_K \boldsymbol{L}_h(\boldsymbol{x}, t) \cdot \boldsymbol{\Phi}_i^{(K)} \, \mathrm{d}\Omega; \; i = 1, \ldots, n_L.$$

The orthonormal Raviart–Thomas basis $\boldsymbol{\eta}_1^{(K)}, \ldots, \boldsymbol{\eta}_{n_{RT}}^{(K)}$ is constructed by mapping to the reference element as $\boldsymbol{\eta}_i^{(K)} = \hat{\boldsymbol{\eta}}_i(\hat{\boldsymbol{x}}^{(K)}(\boldsymbol{x}))$. Here, $\hat{\boldsymbol{x}}^{(K)}(\boldsymbol{x})$ is the mapping from element K to the reference element $\hat{K}$. The reference element $\hat{K}$ is the unit triangle in 2D and the unit tetrahedron in 3D. The functions $\hat{\boldsymbol{\eta}}_1, \ldots, \hat{\boldsymbol{\eta}}_{n_{RT}}$ are an orthonormal Raviart–Thomas basis in the reference element $\hat{K}$. These need to be constructed just once in the reference element. The first dC_d^{k+d} of them are defined simply using the orthonormal polynomial basis as $\hat{\boldsymbol{\eta}}_{(i-1)C_d^{k+d}+j} = \hat{q}_j \boldsymbol{e}_i$, where $j = 1, \ldots, C_d^{k+d}$; $i = 1, \ldots, d$, and $\hat{q}_j$ are the orthonormal Dubiner polynomials that satisfy the orthogonality relation: $\int_{\hat{K}} \hat{q}_i \hat{q}_j \, \mathrm{d}\hat{\Omega} = \delta_{ij} 1/d!$. The last C_{d-1}^{k+d-1} of them, that is, $\hat{\boldsymbol{\eta}}_{dC_d^{k+d}+1}, \ldots, \hat{\boldsymbol{\eta}}_{dC_d^{k+d}+C_{d-1}^{k+d-1}}$, are constructed by multiplying each of the degree k Dubiner polynomials with $\boldsymbol{x}$ and orthonormalizing them against the already computed $\hat{\boldsymbol{\eta}}_i$s using a modified Gram-Schmidt-type procedure.

5.1.3 | Face Velocity

On each face F, the face velocity $\hat{\boldsymbol{u}}_h$ belongs to the function space $\left[P_k(F)\right]^d$. We use the orthonormal basis $\boldsymbol{\psi}_1^{(F)}, \ldots, \boldsymbol{\psi}_{n_{\hat{\boldsymbol{u}}}}^{(F)}$ for this space, where $n_{\hat{\boldsymbol{u}}} = dC_{d-1}^{k+d-1}$ is its dimension. They are defined by mapping the face to a reference face as $\boldsymbol{\psi}_{(i-1)C_{d-1}^{k+d-1}+j}^{(F)} = \hat{w}_j(\hat{\boldsymbol{x}}^{(F)}(\boldsymbol{x}))\boldsymbol{e}_i$, where $j = 1, \ldots, C_{d-1}^{k+d-1}$; $i = 1, \ldots, d$. Here, $\hat{\boldsymbol{x}}^{(F)}(\boldsymbol{x})$ is the mapping from the face F to the reference face $\hat{F}$. The reference face $\hat{F}$ is the unit line in 2D and the unit triangle in 3D. $\hat{w}_k$ are the orthonormal Dubiner polynomials defined on the reference face which satisfy the orthonormality relation $\int_{\hat{F}} \hat{w}_i \hat{w}_j \, \mathrm{d}\hat{\Gamma} = \delta_{ij} \frac{1}{(d-1)!}$. Therefore, the basis functios $\boldsymbol{\psi}_i^{(F)}$ also satisfy the orthonormality relation $\int_F \boldsymbol{\psi}_i^{(F)} \cdot \boldsymbol{\psi}_j^{(F)} \, \mathrm{d}\Gamma = \delta_{ij}|F|$. On face F, the face-velocity $\hat{\boldsymbol{u}}_h(\boldsymbol{x}, t)$ is expanded using this basis as:

$$\hat{\boldsymbol{u}}_h(\boldsymbol{x}, t) = \sum_{i=1}^{n_{\hat{\boldsymbol{u}}}} \hat{\boldsymbol{u}}_{\mathrm{i}}^{(F)}(t) \boldsymbol{\psi}_i^{(F)}(\boldsymbol{x}),$$

$\hat{\boldsymbol{u}}_{\mathrm{i}}^{(F)}(t)$ are the degrees of freedom that depend only on time t and they relate to $\hat{\boldsymbol{u}}_h$ as:

$$\hat{\boldsymbol{u}}_{\mathrm{i}}^{(F)}(t) = \frac{1}{|F|} \int_F \hat{\boldsymbol{u}}_h(\boldsymbol{x}, t) \cdot \boldsymbol{\psi}_i^{(F)}(\boldsymbol{x}) \, \mathrm{d}\Gamma.$$

5.1.4 | Zero-Average Element Pressure

The local problems in Equations (45) to (47) and (48) to (50) need a basis for the zero-average element pressure space $\overline{P}_h(\partial K)$ in each element K. Recall, $\overline{P}_h(\partial K)$ is the set of piecewise polynomials of degree $\leq k$ defined on the boundary ∂K of element K that have zero average on the boundary. We use the basis $\psi_1^{(\partial K)}, \ldots, \psi_{n_p}^{(\partial K)}$ for this space, where $n_p = (d+1)C_{d-1}^{k+d-1} - 1$ is its dimension. The first d piecewise constant basis functions $\psi_1^{(\partial K)}, \ldots, \psi_d^{(\partial K)}$ are defined as:

$$\psi_i^{(\partial K)}(\boldsymbol{x}) = \begin{cases} \frac{|\partial K|}{|F_i|}, & \text{if } \boldsymbol{x} \text{ is on face } F_i \text{ of element } K, \\ -\frac{|\partial K|}{|F_{d+1}|}, & \text{if } \boldsymbol{x} \text{ is on face } F_{d+1} \text{ of element } K, \\ 0, & \text{otherwise,} \end{cases}$$

where $i = 1, \ldots, d$. Note that each of the above basis functions is non-zero on two faces F_i and F_{d+1}. The remaining basis functions $\psi_{d+1}^{(\partial K)}, \ldots, \psi_{n_p}^{(\partial K)}$ are defined piecewisely on each face by mapping it to the reference face as

$$\psi_{d+(i-1)(C_{d-1}^{k+d-1}-1)+(j-1)}^{(\partial K)} = \begin{cases} \hat{w}_j(\hat{\boldsymbol{x}}^{(F_i)}(\boldsymbol{x})), & \text{if } \boldsymbol{x} \text{ is on face } F_i \text{ of element } K, \\ 0, & \text{otherwise,} \end{cases}$$

where $i = 1, \ldots, d+1$, and $j = 2, \ldots, C_{d-1}^{k+d-1}$. These remaining basis functions are non-zero only on one face and have zero average because $\hat{w}_j$ is orthogonal to the constant function "1" for $j \geq 2$.

5.2 | Local Problems

With the above choice of the basis for the different function spaces, the two elementwise maps $(\boldsymbol{u}_{\hat{\boldsymbol{u}}}, \boldsymbol{L}_{\hat{\boldsymbol{u}}}, p_{\hat{\boldsymbol{u}}})$ and $(\boldsymbol{u}_g, \boldsymbol{L}_g, p_g)$ become the below matrices that map one set of degrees of freedom to another. In element K, the matrix form of the mapping $(\boldsymbol{u}_{\hat{\boldsymbol{u}}}, \boldsymbol{L}_{\hat{\boldsymbol{u}}}, p_{\hat{\boldsymbol{u}}})$ is

$$\begin{bmatrix} [\boldsymbol{u}_{\hat{\boldsymbol{u}}}] \\ [\boldsymbol{L}_{\hat{\boldsymbol{u}}}] \\ [p_{\hat{\boldsymbol{u}}}] \end{bmatrix} = \begin{bmatrix} [\boldsymbol{u}_{\hat{\boldsymbol{u}}}]_{1,1} & \cdots & [\boldsymbol{u}_{\hat{\boldsymbol{u}}}]_{1,n_{\hat{\boldsymbol{u}}}} & \cdots & [\boldsymbol{u}_{\hat{\boldsymbol{u}}}]_{1,dn_{\hat{\boldsymbol{u}}}+1} & \cdots & [\boldsymbol{u}_{\hat{\boldsymbol{u}}}]_{1,(d+1)n_{\hat{\boldsymbol{u}}}} \\ \vdots & \cdots & \vdots & \cdots & \vdots & \cdots & \vdots \\ [\boldsymbol{u}_{\hat{\boldsymbol{u}}}]_{n_u,1} & \cdots & [\boldsymbol{u}_{\hat{\boldsymbol{u}}}]_{n_u,n_{\hat{\boldsymbol{u}}}} & \cdots & [\boldsymbol{u}_{\hat{\boldsymbol{u}}}]_{n_u,dn_{\hat{\boldsymbol{u}}}+1} & \cdots & [\boldsymbol{u}_{\hat{\boldsymbol{u}}}]_{n_u,(d+1)n_{\hat{\boldsymbol{u}}}} \\ [\boldsymbol{L}_{\hat{\boldsymbol{u}}}]_{1,1} & \cdots & [\boldsymbol{L}_{\hat{\boldsymbol{u}}}]_{1,n_{\hat{\boldsymbol{u}}}} & \cdots & [\boldsymbol{L}_{\hat{\boldsymbol{u}}}]_{1,dn_{\hat{\boldsymbol{u}}}+1} & \cdots & [\boldsymbol{L}_{\hat{\boldsymbol{u}}}]_{1,(d+1)n_{\hat{\boldsymbol{u}}}} \\ \vdots & \cdots & \vdots & \cdots & \vdots & \cdots & \vdots \\ [\boldsymbol{L}_{\hat{\boldsymbol{u}}}]_{n_L,1} & \cdots & [\boldsymbol{L}_{\hat{\boldsymbol{u}}}]_{n_L,n_{\hat{\boldsymbol{u}}}} & \cdots & [\boldsymbol{L}_{\hat{\boldsymbol{u}}}]_{n_L,dn_{\hat{\boldsymbol{u}}}+1} & \cdots & [\boldsymbol{L}_{\hat{\boldsymbol{u}}}]_{n_L,(d+1)n_{\hat{\boldsymbol{u}}}} \\ \vdots & \cdots & \vdots & \cdots & \vdots & \cdots & \vdots \\ [p_{\hat{\boldsymbol{u}}}]_{1,1} & \cdots & [p_{\hat{\boldsymbol{u}}}]_{1,n_{\hat{\boldsymbol{u}}}} & \cdots & [p_{\hat{\boldsymbol{u}}}]_{1,dn_{\hat{\boldsymbol{u}}}+1} & \cdots & [p_{\hat{\boldsymbol{u}}}]_{1,(d+1)n_{\hat{\boldsymbol{u}}}} \\ \vdots & \cdots & \vdots & \cdots & \vdots & \cdots & \vdots \\ [p_{\hat{\boldsymbol{u}}}]_{n_p,1} & \cdots & [p_{\hat{\boldsymbol{u}}}]_{n_p,n_{\hat{\boldsymbol{u}}}} & \cdots & [p_{\hat{\boldsymbol{u}}}]_{n_p,dn_{\hat{\boldsymbol{u}}}+1} & \cdots & [p_{\hat{\boldsymbol{u}}}]_{n_p,(d+1)n_{\hat{\boldsymbol{u}}}} \end{bmatrix}. \tag{56}$$

Here, $[\boldsymbol{u}_{\hat{u}}]$, $[\boldsymbol{L}_{\hat{u}}]$, and $[p_{\hat{u}}]$ are matrices that map the degrees of freedom of $\boldsymbol{\mu}$ to the degrees of freedom of $\boldsymbol{u}_{\hat{u}}(\boldsymbol{\mu})$, $\boldsymbol{L}_{\hat{u}}(\boldsymbol{\mu})$, and $p_{\hat{u}}(\boldsymbol{\mu})$, respectively. The degrees of freedom of $\boldsymbol{\mu}$ is given by the vector

$$\left[\mu_1^{(F_1)} \ \cdots \ \mu_{n_{\hat{u}}}^{(F_1)} \ \cdots \ \mu_1^{(F_{d+1})} \ \cdots \ \mu_{n_{\hat{u}}}^{(F_{d+1})}\right]^T$$

where $F_1, \ldots, F_{d+1}$ are the faces of element K. The $((j-1)n_{\hat{u}}+\ell)^{th}$ column of the matrices $[\boldsymbol{u}_{\hat{u}}]$, $[\boldsymbol{L}_{\hat{u}}]$, and $[p_{\hat{u}}]$ are the degrees of freedom of $\boldsymbol{u}_{\hat{u}}(\boldsymbol{\mu})$, $\boldsymbol{L}_{\hat{u}}(\boldsymbol{\mu})$, and $p_{\hat{u}}(\boldsymbol{\mu})$, respectively, obtained by setting $\boldsymbol{\mu} = \boldsymbol{\psi}_{\ell}^{(F_j)}$. The linear algebra problem for the matrices $[\boldsymbol{u}_{\hat{u}}]$, $[\boldsymbol{L}_{\hat{u}}]$, and $[p_{\hat{u}}]$ is then

$$\begin{bmatrix} |K|[I]_{n_L\times n_L} & [G_L] & [O]_{n_L\times n_p} \\ -\nu[G_L]^T & \frac{2|K|}{\Delta t}[I]_{n_u\times n_u} & [G_p] \\ [O]_{n_p\times n_L} & [G_p]^T & [O]_{n_p\times n_p} \end{bmatrix} \begin{bmatrix} [\boldsymbol{L}_{\hat{u}}] \\ [\boldsymbol{u}_{\hat{u}}] \\ [p_{\hat{u}}] \end{bmatrix} = \begin{bmatrix} [b(\boldsymbol{L}_{\hat{u}})] \\ [O]_{n_u\times(d+1)n_{\hat{u}}} \\ [b(p_{\hat{u}})] \end{bmatrix} \tag{57}$$

Here, $[I]_{m\times n}$ is a identity matrix of size $m\times n$. $[O]_{m\times n}$ is a zero matrix of size $m\times n$. $[G_L]$ and $[G_p]$ are the gradient matrices associated with the velocity gradient and pressure, respectively. $[b(\boldsymbol{L}_{\hat{u}})]$ and $[b(p_{\hat{u}})]$ are the right-hand side matrices. They are given by

$$\begin{aligned} [G_L]_{i,j} &= \int_K \boldsymbol{\varphi}_j^{(K)} \cdot \left(\boldsymbol{\nabla}\cdot\boldsymbol{\Phi}_i^{(K)}\right)\mathrm{d}\Omega, \ [G_p]_{i,j} = \int_{\partial K} \psi_j^{(\partial K)}\, \boldsymbol{\varphi}_i^{(K)}\cdot\boldsymbol{n}\ \mathrm{d}\Gamma, \\ [b(\boldsymbol{L}_{\hat{u}})]_{i,(j-1)n_{\hat{u}}+\ell} &= \int_{F_j} \boldsymbol{\psi}_{\ell}^{(F_j)}\cdot\left(\boldsymbol{\Phi}_i^{(K)}\boldsymbol{n}\right) d\Gamma, \text{ and } [b(p_{\hat{u}})]_{i,(j-1)n_{\hat{u}}+\ell} \\ &= \int_{\partial K}\left(\boldsymbol{\psi}_{\ell}^{(F_j)}\cdot\boldsymbol{n}\right)\psi_i^{(\partial K)}\, d\Gamma. \end{aligned} \tag{58}$$

Note that the mass matrices corresponding to the velocity gradient and velocity in Equation (57) are diagonal matrices. This is because our basis functions are orthogonal. We exploit this to efficiently solve the above system of equations by static condensation.

Similarly, the matrix form of the other map ($\boldsymbol{u}_g$, $\boldsymbol{L}_g$, p_g) in element K is

$$\begin{bmatrix} [\boldsymbol{u}_g] \\ [\boldsymbol{L}_g] \\ [p_g] \end{bmatrix} = \begin{bmatrix} [\boldsymbol{u}_g]_{1,1} & \cdots & [\boldsymbol{u}_g]_{1,n_u} \\ \vdots & \cdots & \vdots \\ [\boldsymbol{u}_g]_{n_u,1} & \cdots & [\boldsymbol{u}_g]_{n_u,n_u} \\ [\boldsymbol{L}_g]_{1,1} & \cdots & [\boldsymbol{L}_g]_{1,n_u} \\ \vdots & \cdots & \vdots \\ [\boldsymbol{L}_g]_{n_L,1} & \cdots & [\boldsymbol{L}_g]_{n_L,n_u} \\ \vdots & \cdots & \vdots \\ [p_g]_{1,1} & \cdots & [p_g]_{1,n_u} \\ \vdots & \cdots & \vdots \\ [p_g]_{n_p,1} & \cdots & [p_g]_{n_p,n_u} \end{bmatrix}. \tag{59}$$

The matrices $[\boldsymbol{u}_g]$, $[\boldsymbol{L}_g]$, and $[p_g]$ map the degree of freedom of $\boldsymbol{f}$ to the degrees of freedom of $\boldsymbol{u}_g(\boldsymbol{f})$, $\boldsymbol{L}_g(\boldsymbol{f})$, and $p_g(\boldsymbol{f})$, respectively. The linear algebra problem for the matrices $[\boldsymbol{u}_g]$, $[\boldsymbol{L}_g]$ is

$$\begin{bmatrix} |K|[I]_{n_L\times n_L} & [G_L] & [O]_{n_L\times n_p} \\ -\nu[G_L]^T & \frac{2|K|}{\Delta t}[I]_{n_u\times n_u} & [G_p] \\ [O]_{n_p\times n_L} & [G_p]^T & [O]_{n_p\times n_p} \end{bmatrix} \begin{bmatrix} [\boldsymbol{L}_g] \\ [\boldsymbol{u}_g] \\ [p_g] \end{bmatrix} = \begin{bmatrix} [O]_{n_L\times n_u} \\ |K|[I]_{n_u\times n_u} \\ [O]_{n_p\times n_u} \end{bmatrix}. \tag{60}$$

All the matrices above are defined in Equation (57).

5.3 | Global Problem

With the above basis functions, the global problem for $\hat{\boldsymbol{u}}_h^n$ and $\overline{p}_{h,\partial K}^{n-\frac{1}{2}}$ becomes the below matrix problem:

$$\begin{bmatrix} [A_{\hat{u}}] & -[G_{\overline{p}}] \\ [G_{\overline{p}}]^T & [O]_{n_K\times n_K} \end{bmatrix} \begin{bmatrix} \{\hat{\boldsymbol{u}}_i^{(F)^{n-\frac{1}{2}}}\} \\ \{\overline{p}_{h,\partial K}^{n-\frac{1}{2}}\} \end{bmatrix} = \begin{bmatrix} b(\hat{\boldsymbol{u}}_h^{n-\frac{1}{2}}) \\ [O]_{n_K\times 1} \end{bmatrix}$$

Here, n_K is the number of elements in the mesh. $[A_{\hat{u}}]$ is the sparse effective stiffness matrix and $[G_{\overline{p}}]$ is the sparse gradient matrix corresponding to the average pressure. $b(\hat{\boldsymbol{u}}_h^{n-\frac{1}{2}})$ is the right-hand side vector. $\{\hat{\boldsymbol{u}}_i^{(F)^{n-\frac{1}{2}}}\}$ and $\{\overline{p}_{h,\partial K}\}$ are the left-hand side vectors comprising of the degrees of freedom of $\hat{\boldsymbol{u}}_h^{n-\frac{1}{2}}$ and $\overline{p}_{h,\partial K}$, respectively. The effective stiffness matrix $[A_{\hat{u}}]$, the gradient matrix $[G_{\overline{p}}]$ and the right-hand side vector $b(\hat{\boldsymbol{u}}_h^{n-\frac{1}{2}})$ are formed by assembling the element effective stiffness matrix $\left[A_{\hat{u}}^{(K)}\right]$ (size $dn_{\hat{u}}\times dn_{\hat{u}}$), element gradient vector $\left[G_{\overline{p}}^{(K)}\right]$ (size $dn_{\hat{u}}\times 1$), and element vector $b^{(K)}(\hat{\boldsymbol{u}}_h^{n-\frac{1}{2}})$ (size $dn_{\hat{u}}\times 1$), respectively. They are given by

$$\begin{aligned} \left[A_{\hat{u}}^{(K)}\right] &= \nu|K|[\boldsymbol{L}_{\hat{u}}]^T[\boldsymbol{L}_{\hat{u}}] + \frac{2}{\Delta t}[\boldsymbol{u}_{\hat{u}}]^T[\boldsymbol{u}_{\hat{u}}], \ b^{(K)}(\hat{\boldsymbol{u}}_h^{n-\frac{1}{2}}) \\ &= |K|[\boldsymbol{u}_{\hat{u}}]^T\{\boldsymbol{g}_i^{n-\frac{1}{2}}\}, \text{ and the only non-zero entries in} \\ \left[G_{\overline{p}}^{(K)}\right] &\text{ are } \left[G_{\overline{p}}^{(K)}\right]_{(j-1)n_{\hat{u}}+(i-1)C_{d-1}^{k+d-1}+1,1} = n_i^{(F_j)}|F_j|, \\ &\text{for } i = 1, \ldots, d; j = 1, \ldots, d+1. \end{aligned}$$

Here, $[\boldsymbol{L}_{\hat{u}}]$ and $[\boldsymbol{u}_{\hat{u}}]$ are the elementwise matrices that we defined in the previous subsection, and $\{\boldsymbol{g}_i^{n-\frac{1}{2}}\}$ is the degree of freedom vector of the elementwise net body force $\boldsymbol{g}_h^{n-\frac{1}{2}}$. We note that because our basis functions are orthonormal, we have terms above that are products of two matrices, that is, the terms $[\boldsymbol{L}_{\hat{u}}]^T[\boldsymbol{L}_{\hat{u}}]$, $[\boldsymbol{u}_{\hat{u}}]^T[\boldsymbol{u}_{\hat{u}}]$, and $[\boldsymbol{u}_{\hat{u}}]^T\{\boldsymbol{g}_h^{n-\frac{1}{2}}\}$. If they were not orthonormal, we would have products of three matrices instead, that is, the terms would have been $[\boldsymbol{L}_{\hat{u}}]^T M_L[\boldsymbol{L}_{\hat{u}}]$, $[\boldsymbol{u}_{\hat{u}}]^T M_u[\boldsymbol{u}_{\hat{u}}]$, and $[\boldsymbol{u}_{\hat{u}}]^T M_u\{\boldsymbol{g}_h^{n-\frac{1}{2}}\}$ instead, and their computation would have been more expensive. M_L and M_u are the fully dense mass matrices from the non-orthonormal basis. The expression for $\boldsymbol{g}_i^{n-\frac{1}{2}}$ is

$$\begin{aligned} \boldsymbol{g}_i^{n-\frac{1}{2}} &= \frac{1}{|K|}\int_K \boldsymbol{f}^{n-\frac{1}{2}}\cdot\boldsymbol{\varphi}_i\, d\Omega + \frac{1}{|K|}\int_K\left(\frac{3}{2}\boldsymbol{u}_h^{n-1}\otimes\boldsymbol{u}_h^{n-1} - \frac{1}{2}\boldsymbol{u}_h^{n-2}\otimes\boldsymbol{u}_h^{n-2}\right) \\ &\quad\cdot\boldsymbol{\nabla}\boldsymbol{\varphi}_i\ \mathrm{d}\Omega \\ &\quad - \frac{1}{|K|}\sum_{F\in\partial K}\int_F\left(\frac{3}{2}\boldsymbol{f}_{h,c}(\hat{\boldsymbol{u}}_h^{n-1},\hat{\boldsymbol{u}}_{T,h}^{n-1}) - \frac{1}{2}\boldsymbol{f}_{h,c}(\hat{\boldsymbol{u}}_h^{n-2},\hat{\boldsymbol{u}}_{T,h}^{n-2})\right)\cdot\boldsymbol{\varphi}_i\ \mathrm{d}\Gamma + \frac{2}{\Delta t}\boldsymbol{u}_i^{n-1} \end{aligned} \tag{61}$$

While assembling, we also replace the face velocity degrees of freedom for the Dirichlet boundary faces with that computed using Equation (54) and statically condense these degrees of freedom.

5.4 | Quadrature Rules

The integrals are computed using the standard Duffy transform. The integrals over a line, triangle, and tetrahedron are computed

by mapping them to a unit line, unit square, and unit cube, respectively. We use $(k+1)$ points along each direction for all the integrals in Equations (58) and (61) except the non-linear convective term integrals. To evaluate these non-linear integrals, we use $(3k+1)/2$ points (rounded up) in each direction.

5.5 | Initial Condition

The initial element velocity $\boldsymbol{u}_h^0$ and face velocity $\hat{\boldsymbol{u}}_h^0$ are computed from the exact initial velocity $\boldsymbol{u}(\boldsymbol{x}, t=0)$ such that $\boldsymbol{u}_h^0$ is $H(\mathrm{div})$-conforming and exactly divergence-free. This procedure also enforces the normal component of these two initial velocities to be equal to each other on the mesh faces. First, the initial face velocity $\hat{\boldsymbol{u}}_h^0$ is computed by projecting $\boldsymbol{u}(\boldsymbol{x}, t=0)$ on each face F as $\int_F \hat{\boldsymbol{u}}_h^0 \cdot \boldsymbol{\mu}_h \, \mathrm{d}\Gamma = \int_F \boldsymbol{u}(\boldsymbol{x}, t=0) \cdot \boldsymbol{\mu}_h \, \mathrm{d}\Gamma$, for all test functions $\boldsymbol{\mu}_h$ in $\boldsymbol{M}_h$. Then, we compute the initial element velocity $\boldsymbol{u}_h^0$ by projecting $\boldsymbol{u}(\boldsymbol{x}, t=0)$ in each element K while requiring the normal components of $\boldsymbol{u}_h^0$ and $\hat{\boldsymbol{u}}_h^0$ to be equal to each other on the element faces as

$$\int_K \boldsymbol{u}_h^0 \cdot \boldsymbol{v} \, \mathrm{d}\Omega + \sum_{F \in \partial K} \int_F \lambda_h \, \boldsymbol{v} \cdot \boldsymbol{n} \, \mathrm{d}\Gamma = \int_K \boldsymbol{u}(\boldsymbol{x}, t=0) \cdot \boldsymbol{v} \, \mathrm{d}\Omega,$$

$$\sum_{F \in \partial K} \int_F \boldsymbol{u}_h^0 \cdot \boldsymbol{n} \, q \, \mathrm{d}\Gamma = \sum_{F \in \partial K} \int_F \hat{\boldsymbol{u}}_h^0 \cdot \boldsymbol{n} \, q \, \mathrm{d}\Gamma,$$

for all test functions $\boldsymbol{v}$ and q in $\boldsymbol{V}_h(K)$ and $\overline{P}_h(\partial K)$, respectively.

6 | Analysis

6.1 | Continuity of Stresses

We show that the normal component of $\nu \boldsymbol{L}_h^{n-\frac{1}{2}} - p_h^{n-\frac{1}{2}} \boldsymbol{I}$ is continuous across the interior faces. On these faces, they satisfy the weak continuity condition given in Equation (37):

$$\int_{F_I} \left[\left(\nu \boldsymbol{L}_h^{n-\frac{1}{2}^+} - p_h^{n-\frac{1}{2}^+} \boldsymbol{I} \right) \boldsymbol{n}^+ + \left(\nu \boldsymbol{L}_h^{n-\frac{1}{2}^-} - p_h^{n-\frac{1}{2}^-} \boldsymbol{I} \right) \boldsymbol{n}^- \right] \cdot \boldsymbol{\mu} \, \mathrm{d}\Gamma = 0, \text{for all } \boldsymbol{\mu} \text{ belonging to } \left[P_k(F_I) \right]^d$$

$\left[\left(\nu \boldsymbol{L}_h^{n-\frac{1}{2}^+} - p_h^{n-\frac{1}{2}^+} \boldsymbol{I} \right) \boldsymbol{n}^+ + \left(\nu \boldsymbol{L}_h^{n-\frac{1}{2}^-} - p_h^{n-\frac{1}{2}^-} \boldsymbol{I} \right) \boldsymbol{n}^- \right]$ is infact a function in $\left[P_k(F_I) \right]^d$. Therefore, choosing $\boldsymbol{\mu}$ to be equal to this function, we obtain

$$\int_{F_I} \left\| \left(\nu \boldsymbol{L}_h^{n-\frac{1}{2}^+} - p_h^{n-\frac{1}{2}^+} \boldsymbol{I} \right) \boldsymbol{n}^+ + \left(\nu \boldsymbol{L}_h^{n-\frac{1}{2}^-} - p_h^{n-\frac{1}{2}^-} \boldsymbol{I} \right) \boldsymbol{n}^- \right\|_2^2 \mathrm{d}\Gamma = 0.$$

Therefore, the normal component of $\nu \boldsymbol{L}_h^{n-\frac{1}{2}} - p_h^{n-\frac{1}{2}} \boldsymbol{I}$ is continuous across the interior faces.

6.2 | Mass Conservation

We show that the element velocity $\boldsymbol{u}_h^n$ computed using our method is pointwise divergence-free and $H(\mathrm{div})$-conforming. The former property is automatically satisfied because we use the pointwise divergence-free polynomial space $\boldsymbol{V}_h(K)$ for $\boldsymbol{u}_h^n$ in element K. To show that $\boldsymbol{u}_h^n$ is $H(\mathrm{div})$-conforming, we have to show that its normal component is continuous across the element boundaries. Consider Equation (35). Using the definition of $\boldsymbol{u}_h^{n-\frac{1}{2}}$, we obtain that

$$\sum_{F \in \partial K} \int_F \left(\boldsymbol{u}_h^{n-\frac{1}{2}} \cdot \boldsymbol{n} - \hat{\boldsymbol{u}}_h^{n-\frac{1}{2}} \cdot \boldsymbol{n} \right) q \, \mathrm{d}\Gamma = 0$$

for all test functions q in the function space $P_h(\partial K)$.

Choosing q on each face F to be $\boldsymbol{u}_h^{n-\frac{1}{2}} \cdot \boldsymbol{n} - \hat{\boldsymbol{u}}_h^{n-\frac{1}{2}} \cdot \boldsymbol{n}$ yields

$$\sum_{F \in \partial K} \int_F \left(\boldsymbol{u}_h^{n-\frac{1}{2}} \cdot \boldsymbol{n} - \hat{\boldsymbol{u}}_h^{n-\frac{1}{2}} \cdot \boldsymbol{n} \right)^2 \mathrm{d}\Gamma = 0.$$

Hence, $\boldsymbol{u}_h^{n-\frac{1}{2}} \cdot \boldsymbol{n} = \hat{\boldsymbol{u}}_h^{n-\frac{1}{2}} \cdot \boldsymbol{n}$. Furthermore, since $\hat{\boldsymbol{u}}_h^{n-\frac{1}{2}}$ is single valued on a face, we have $\boldsymbol{u}_h^{n-\frac{1}{2}^+} \cdot \boldsymbol{n}^+ + \boldsymbol{u}_h^{n-\frac{1}{2}^-} \cdot \boldsymbol{n}^- = 0$. Therefore, the normal component of the $\boldsymbol{u}_h^{n-\frac{1}{2}}$ is continuous across elements. This implies that if the normal components of $\boldsymbol{u}_h^{n-1}$ are continuous, then the normal components of $\boldsymbol{u}_h^n$ are also continuous. Since the normal components of the initial element velocity $\boldsymbol{u}_h^0$ are continuous, by induction, we obtain that the normal components of $\boldsymbol{u}_h^n$ are continuous. Finally, we note that because the velocity is pointwise divergence-free and $H(\mathrm{div})$-conforming, we discretely conserve mass locally (and globally).

6.3 | Momentum Conservation

We show that our method locally (and globally) conserves the discrete momentum. Consider Equation (34). Substituting $\boldsymbol{v} = \boldsymbol{e}_i$, we obtain the below evolution equation for the integrated momentum in element K:

$$\int_K \frac{\boldsymbol{u}_h^n - \boldsymbol{u}_h^{n-1}}{\Delta t} \cdot \boldsymbol{e}_i \, \mathrm{d}\Omega + \sum_{F \in \partial K} \int_F \left(\frac{3}{2} \boldsymbol{f}_{h,c}(\hat{\boldsymbol{u}}_h^n, \hat{\boldsymbol{u}}_{T,h}^n) - \frac{1}{2} \boldsymbol{f}_{h,c}(\hat{\boldsymbol{u}}_h^{n-1}, \hat{\boldsymbol{u}}_{T,h}^{n-1}) \right) \cdot \boldsymbol{e}_i \, \mathrm{d}\Gamma = \sum_{F \in \partial K} \int_F (\nu \boldsymbol{L}_h^{n-\frac{1}{2}} - p_h^{n-\frac{1}{2}} \boldsymbol{I}) \boldsymbol{n} \cdot \boldsymbol{e}_i \, \mathrm{d}\Gamma + \int_K \boldsymbol{f}^{n-\frac{1}{2}} \cdot \boldsymbol{e}_i \, \mathrm{d}\Omega. \tag{62}$$

The numerical convective flux $\boldsymbol{f}_{h,c}$ and the normal component of the $\nu \boldsymbol{L}_h^{n-\frac{1}{2}} - p_h^{n-\frac{1}{2}} \boldsymbol{I}$ are continuous across the interior faces, that is, they satisfy

$$\boldsymbol{f}_{h,c}^+ + \boldsymbol{f}_{h,c}^- = 0, \text{ and } \left(\nu \boldsymbol{L}_h^{n-\frac{1}{2}^+} - p_h^{n-\frac{1}{2}^+} \boldsymbol{I} \right) \boldsymbol{n}^+ + \left(\nu \boldsymbol{L}^{n-\frac{1}{2}^-} - p_h^{n-\frac{1}{2}^-} \boldsymbol{I} \right) \boldsymbol{n}^- = 0.$$

Therefore, when Equation (62) is summed over a set of elements, the contribution from faces that are interior to the set cancels to zero. Only the contribution from faces that are on the boundary of the set remains. Hence, our method locally (and as well as globally) conserves the discrete momentum.

6.4 | Kinetic Energy Conservation

We show below that our spatial discretization locally (and globally) conserves the discrete kinetic energy. Consider

Equations (22) to (24). Substituting $\boldsymbol{v} = \boldsymbol{u}_h$, $\boldsymbol{G} = \nu \boldsymbol{L}_h$ and $q = p_h$ and manipulating the three equations into one, we obtain

$$\begin{aligned}
&\frac{d}{dt}\int_K \frac{\boldsymbol{u}_h \cdot \boldsymbol{u}_h}{2}\,\mathrm{d}\Omega - \int_K (\boldsymbol{u}_h \otimes \boldsymbol{u}_h) \cdot \boldsymbol{\nabla} \boldsymbol{u}_h\,\mathrm{d}\Omega \\
&\quad + \sum_{F\in\partial K}\int_F \boldsymbol{f}_{h,c}(\hat{\boldsymbol{u}}_h, \hat{\boldsymbol{u}}_{T,h}) \cdot \boldsymbol{u}_h\,\mathrm{d}\Gamma \\
&= \sum_{F\in\partial K}\int_F (\nu \boldsymbol{L}_h - p_h \boldsymbol{I})\boldsymbol{n} \cdot \hat{\boldsymbol{u}}_h\,\mathrm{d}\Gamma - \nu\int_K \boldsymbol{L}_h \cdot \boldsymbol{L}_h\,\mathrm{d}\Omega + \int_K \boldsymbol{f} \cdot \boldsymbol{u}_h\,\mathrm{d}\Omega.
\end{aligned} \tag{63}$$

Since $\hat{\boldsymbol{u}}$ is pointwise divergence-free and $\boldsymbol{u}_h \cdot \boldsymbol{n} = \hat{\boldsymbol{u}}_h \cdot \boldsymbol{n}$ on the element faces (obtained by setting $q = \boldsymbol{u}_h \cdot \boldsymbol{n} - \hat{\boldsymbol{u}}_h \cdot \boldsymbol{n}$ in Equation (24)), we have

$$\int_K (\boldsymbol{u}_h \otimes \boldsymbol{u}_h) \cdot \boldsymbol{\nabla} \boldsymbol{u}_h\,\mathrm{d}\Omega = \sum_{F\in\partial K}\int_F \frac{\boldsymbol{u}_h \cdot \boldsymbol{u}_h}{2}\hat{\boldsymbol{u}}_h \cdot \boldsymbol{n}\,\mathrm{d}\Gamma.$$

Splitting $\boldsymbol{u}_h \cdot \boldsymbol{u}_h$ into normal and tangential components and using $\boldsymbol{u}_h \cdot \boldsymbol{n} = \hat{\boldsymbol{u}}_h \cdot \boldsymbol{n}$ yields

$$\begin{aligned}
\int_K (\boldsymbol{u}_h \otimes \boldsymbol{u}_h) \cdot \boldsymbol{\nabla} \boldsymbol{u}_h\,\mathrm{d}\Omega &= \sum_{F\in\partial K}\int_F \frac{|\hat{\boldsymbol{u}}_h \cdot \boldsymbol{n}|^2}{2}\hat{\boldsymbol{u}}_h \cdot \boldsymbol{n}\,\mathrm{d}\Gamma \\
&\quad + \sum_{F\in\partial K}\int_F \frac{\boldsymbol{u}_{h,T} \cdot \boldsymbol{u}_{h,T}}{2}\hat{\boldsymbol{u}}_h \cdot \boldsymbol{n}\,\mathrm{d}\Gamma.
\end{aligned} \tag{64}$$

Substituting for $\boldsymbol{f}_{h,c}$, we obtain that

$$\begin{aligned}
&\sum_{F\in\partial K}\int_F \boldsymbol{f}_{h,c}(\hat{\boldsymbol{u}}_h, \hat{\boldsymbol{u}}_{T,h}) \cdot \boldsymbol{u}_h\,\mathrm{d}\Gamma \\
&= \sum_{F\in\partial K}\int_F (\hat{\boldsymbol{u}}_h \cdot \boldsymbol{n})(\hat{\boldsymbol{u}}_{h,T} + (\hat{\boldsymbol{u}}_h \cdot \boldsymbol{n})\boldsymbol{n}) \cdot \boldsymbol{u}_h\,\mathrm{d}\Gamma
\end{aligned}$$

Splitting $\boldsymbol{u}_h$ into $(\hat{\boldsymbol{u}}_h \cdot \boldsymbol{n})\boldsymbol{n} + \boldsymbol{u}_{h,T}$ and using $\boldsymbol{u}_h \cdot \boldsymbol{n} = \hat{\boldsymbol{u}}_h \cdot \boldsymbol{n}$ yields

$$\begin{aligned}
\sum_{F\in\partial K}\int_F \boldsymbol{f}_{h,c}(\hat{\boldsymbol{u}}_h, \hat{\boldsymbol{u}}_{T,h}) \cdot \boldsymbol{u}_h\,\mathrm{d}\Gamma &= \sum_{F\in\partial K}\int_F |\hat{\boldsymbol{u}}_h \cdot \boldsymbol{n}|^2 \hat{\boldsymbol{u}}_h \cdot \boldsymbol{n}\,\mathrm{d}\Gamma \\
&\quad + \sum_{F\in\partial K}\int_F (\hat{\boldsymbol{u}}_{h,T} \cdot \boldsymbol{u}_{h,T})\hat{\boldsymbol{u}}_h \cdot \boldsymbol{n}\,\mathrm{d}\Gamma.
\end{aligned} \tag{65}$$

Substituting Equations (64) and (65) into Equation (63), we obtain

$$\begin{aligned}
&\frac{d}{dt}\int_K \frac{\boldsymbol{u}_h \cdot \boldsymbol{u}_h}{2}\,\mathrm{d}\Omega + \underbrace{\sum_{F\in\partial K}\int_F \frac{|\hat{\boldsymbol{u}}_h \cdot \boldsymbol{n}|^2}{2}\hat{\boldsymbol{u}}_h \cdot \boldsymbol{n}\,\mathrm{d}\Gamma}_{\text{term 1}} \\
&+ \underbrace{\sum_{F\in\partial K}\int_F \left(\hat{\boldsymbol{u}}_{h,T} \cdot \boldsymbol{u}_{h,T} - \frac{\boldsymbol{u}_{h,T} \cdot \boldsymbol{u}_{h,T}}{2}\right)\hat{\boldsymbol{u}}_h \cdot \boldsymbol{n}\,\mathrm{d}\Gamma}_{\text{term 2}} \\
&= \underbrace{\sum_{F\in\partial K}\int_F (\nu \boldsymbol{L}_h - p_h \boldsymbol{I})\boldsymbol{n} \cdot \hat{\boldsymbol{u}}_h\,\mathrm{d}\Gamma}_{\text{term 3}} - \nu\int_K \boldsymbol{L}_h \cdot \boldsymbol{L}_h\,\mathrm{d}\Omega + \int_K \boldsymbol{f} \cdot \boldsymbol{u}_h\,\mathrm{d}\Omega.
\end{aligned} \tag{66}$$

On the interior faces, we have the relations:

$$\nu(\boldsymbol{L}_h^+ - p_h^+ \boldsymbol{I})\boldsymbol{n}^+ \cdot \hat{\boldsymbol{u}}_h + \nu(\boldsymbol{L}_h^- - p_h^- \boldsymbol{I})\boldsymbol{n}^- \cdot \hat{\boldsymbol{u}}_h = 0, \tag{67}$$

$$\frac{|\hat{\boldsymbol{u}}_h \cdot \boldsymbol{n}^+|^2}{2}\hat{\boldsymbol{u}}_h \cdot \boldsymbol{n}^+ + \frac{|\hat{\boldsymbol{u}}_h \cdot \boldsymbol{n}^-|^2}{2}\hat{\boldsymbol{u}}_h \cdot \boldsymbol{n}^- = 0, \text{ and} \tag{68}$$

$$\begin{aligned}
&\left(\hat{\boldsymbol{u}}_{h,T} \cdot \boldsymbol{u}_{h,T}^+ - \frac{\boldsymbol{u}_{h,T}^+ \cdot \boldsymbol{u}_{h,T}^+}{2}\right)\hat{\boldsymbol{u}}_h \cdot \boldsymbol{n}^+ + \left(\hat{\boldsymbol{u}}_{h,T} \cdot \boldsymbol{u}_{h,T}^- - \frac{\boldsymbol{u}_{h,T}^- \cdot \boldsymbol{u}_{h,T}^-}{2}\right) \\
&\quad \hat{\boldsymbol{u}}_h \cdot \boldsymbol{n}^- = 0,
\end{aligned} \tag{69}$$

The last relation above is true because, on the interior faces, we set $\hat{\boldsymbol{u}}_{h,T} = (\boldsymbol{u}_{h,T}^+ + \boldsymbol{u}_{h,T}^-)/2$ (Equation (30)). Therefore, when we sum the Equation (66) over a set of elements, the contribution from the interior faces of the set cancels to zero. Only the contribution from the boundary faces of the set remains. Hence, our spatial discretization locally (and globally) conserves the discrete kinetic energy.

Periodic Boundaries. If only periodic boundaries are present, all faces become interior faces. Therefore, summing Equation (66) over all elements yields

$$\frac{d}{dt}\sum_K \int_K \frac{\boldsymbol{u}_h \cdot \boldsymbol{u}_h}{2}\,\mathrm{d}\Omega = -\sum_K \nu\int_K \boldsymbol{L}_h \cdot \boldsymbol{L}_h\,\mathrm{d}\Omega + \sum_K \int_K \boldsymbol{f} \cdot \boldsymbol{u}_h\,\mathrm{d}\Omega.$$

In the inviscid limit ($\nu \to 0$) and no body force ($\boldsymbol{f} = 0$), the integrated kinetic energy is exactly invariant with time, that is,

$$\frac{d}{dt}\sum_K \int_K \frac{\boldsymbol{u}_h \cdot \boldsymbol{u}_h}{2}\,\mathrm{d}\Omega = 0. \tag{70}$$

6.5 | Numerical Tangential Face Velocity on Dirichlet Boundaries

Let K be an element adjacent to the Dirichlet boundary. The discrete kinetic energy evolution (Equation (66)) for this element can be written as

$$\begin{aligned}
\frac{d}{dt}\int_K \frac{\boldsymbol{u}_h \cdot \boldsymbol{u}_h}{2}\,\mathrm{d}\Omega &= \underbrace{-\sum_{F_D\in\partial K\cap\partial\Omega_D}\int_{F_D} \frac{|\hat{\boldsymbol{u}}_h \cdot \boldsymbol{n}|^2}{2}\hat{\boldsymbol{u}}_h \cdot \boldsymbol{n}\,\mathrm{d}\Gamma}_{\text{term 1}} \\
&\quad \underbrace{-\sum_{F_D\in\partial K\cap\partial\Omega_D}\int_{F_D}\left(\hat{\boldsymbol{u}}_{h,T} \cdot \boldsymbol{u}_{h,T} - \frac{\boldsymbol{u}_{h,T} \cdot \boldsymbol{u}_{h,T}}{2}\right)\hat{\boldsymbol{u}}_h \cdot \boldsymbol{n}\,\mathrm{d}\Gamma + \ldots}_{\text{term 2}}
\end{aligned}$$

Here, F_D is a Dirichlet boundary face and $\partial K \cap \partial\Omega_D$ is the set of Dirichlet boundary faces of element K. Term 1 depends only on $\hat{\boldsymbol{u}}_h$ which on the Dirichlet boundary faces F_D is set using the Dirichlet boundary data $\hat{\boldsymbol{u}}_D$. Therefore, term 1 injects and removes energy solely based on the boundary data, and is hence okay for stability. However, term 2 depends on $\hat{\boldsymbol{u}}_{h,T}$, $\boldsymbol{u}_{h,T}$, and $\hat{\boldsymbol{u}}_h$. Hence, its stability is not guaranteed. It depends on how $\hat{\boldsymbol{u}}_{h,T}$ is prescribed on the Dirichlet boundary.

We show below that setting $\hat{\boldsymbol{u}}_{h,T}$ on the Dirichlet boundary faces using Equation (31) stably imposes the Dirichlet boundary condition. Splitting F_D into two portions where $\hat{\boldsymbol{u}}_h \cdot \boldsymbol{n}$ is greater than and less than zero, and using Equation (31) yields

$$-\int_{F_D}\left(\hat{\boldsymbol{u}}_{h,T} \cdot \boldsymbol{u}_{h,T} - \frac{\boldsymbol{u}_{h,T} \cdot \boldsymbol{u}_{h,T}}{2}\right)\hat{\boldsymbol{u}}_h \cdot \boldsymbol{n}\,\mathrm{d}\Gamma$$

$$= \underbrace{-\int_{F_D,\hat{\boldsymbol{u}}_h\cdot\boldsymbol{n}>0} \frac{\|\boldsymbol{u}_{h,T}\|_2^2}{2}\hat{\boldsymbol{u}}_h\cdot\boldsymbol{n}\,\mathrm{d}\Gamma}_{\text{term 3}}$$

$$\underbrace{-\int_{F_D,\hat{\boldsymbol{u}}_h\cdot\boldsymbol{n}<0} \frac{|\hat{\boldsymbol{u}}_h-(\hat{\boldsymbol{u}}_h\cdot\boldsymbol{n})\boldsymbol{n}|^2}{2}\hat{\boldsymbol{u}}_h\cdot\boldsymbol{n}\,\mathrm{d}\Gamma}_{\text{term 4}}$$

$$\underbrace{\int_{F_D,\hat{\boldsymbol{u}}_h\cdot\boldsymbol{n}<0} \frac{|\boldsymbol{u}_{h,T}-(\hat{\boldsymbol{u}}_h-(\hat{\boldsymbol{u}}_h\cdot\boldsymbol{n})\boldsymbol{n})|^2}{2}\hat{\boldsymbol{u}}_h\cdot\boldsymbol{n}\,\mathrm{d}\Gamma}_{\text{term 5}}$$

Similar to term 1, term 4 in the above equation also depends solely on $\hat{\boldsymbol{u}}_h$ and is hence okay for stability. Terms 3 and 5 above are always negative and, therefore, they are also okay for stability. Hence, setting the numerical tangential face velocity on the Dirichlet boundaries using Equation (31) imposes the Dirichlet boundary condition in a stable manner.

7 | Numerical Results

7.1 | Taylor–Green Vortex

The below set of numerical experiments demonstrate the various features of our method using the Taylor–Green vortex problem. The analytical solution is:

$$\boldsymbol{u}(\boldsymbol{x},t) = \left\{\sin(x_1)\cos(x_2)e^{\frac{-2t}{Re}}, -\cos(x_1)\sin(x_2)e^{\frac{-2t}{Re}}\right\} \tag{71}$$

The velocity and length scales are the peak velocity and the inverse wavenumber (2π/wavelength), respectively, of the initial perturbation. The Reynolds number Re is defined based on these two scales.

7.1.1 | Non-Dissipative and Stable at High Reynolds Numbers

We demonstrate that our method is non-dissipative and stable at a high Reynolds number by simulating this problem at a high Reynolds number of 10^9. We run two sets of simulations – one using a uniform mesh (shown in Figure 1a) and the other using a skewed mesh (shown in Figure 1b). For each mesh, we compute the solution for degrees $k = 1$ to 10 up to a non-dimensional time of 10. The computed velocity (x_1-component and time $t = 10$) with degree $k = 10$ for the uniform and skewed meshes are shown in Figure 1a,b, respectively.

The evolution of the discrete kinetic energy with time are plotted for the uniform and skewed meshes in Figure 1c,d, respectively. Also shown is the evolution of the exact kinetic energy. Since the Reynolds number is very high, the exact kinetic energy remains close to the initial kinetic energy at all times. The discrete kinetic energy reproduces this behavior, for all the degrees and both meshes. This reproduction occurs because our numerical scheme is non-dissipative and stable. Non-dissipativity keeps the kinetic energy close to the initial kinetic energy and stability ensures that the simulation does not blow up due to discretization errors. If the scheme was dissipative, then at least for the low polynomial degrees, the discrete kinetic energy would have substantially decayed. If the scheme was unstable, then the kinetic energy would have grown indefinitely.

7.1.2 | Convergence: *p*-Refinement

We study the convergence of our method with increasing polynomial degrees while keeping the mesh fixed, that is, with p-Refinement. This is done for both uniform and skewed meshes (same meshes as the ones used in the previous subsection) and for two Reynolds numbers, 10^2 and 10^9. We compute the velocity until time $t = 1$ for degrees $k = 1$ to 10. Figure 1e–h show the L^∞-error in the computed solution for the different cases. L^∞-error is discretely measured by computing it at 1600 points in each element. The error decays exponentially with polynomial degree, for both uniform and skewed meshes and both Reynolds numbers. As expected, the error in the skewed mesh is more than the uniform mesh. Furthermore, observe that the error is nearly independent of the Reynolds number for both meshes.

7.1.3 | Convergence: *h*-Refinement

We study the convergence of our method with h-Refinement. This is also done for both uniform and skewed meshes. The uniform meshes use a $2N$ number of triangular elements along each direction. The skewed meshes are constructed by mapping each node of the uniform mesh using the relation:

$$(x, y) \to (x + \alpha\sin(y), y + \alpha\sin(x)).$$

Here, α is a parameter that controls the skewness of the mesh. Larger the value of α, larger is the skewness. We set α to 0.5. The values of N considered are 2, 4, 8, 16, and 32. We run the problem for 10 time steps with a very small time step of 10^{-6} and measure the discrete L^∞-error at the end of the 10^{th} timestep. Choosing a very small time step isolates just the spatial discretization error. Two Reynolds numbers, 10^2 and 10^9, are considered. Each of these problems is simulated for polynomial degrees 1 to 6.

Figure 2 shows the L^∞-error (maximum of $\boldsymbol{u}_1$ and $\boldsymbol{u}_2$) as a function of the mesh size (proportional to $1/N$) for the different cases. The error decays as Ch^{k+1} for all the cases. Further, the constant C depends on the mesh but does not appear to depend much on the Reynolds number.

7.2 | Convecting Taylor–Green Vortex at High Reynolds Numbers

We below demonstrate the accuracy of our numerical method at high Reynolds numbers when convection is involved. We simulate the convecting Taylor–Green vortex problem. The vortex is assumed to convect only in the x_1-direction. Its analytical solution is:

$$\boldsymbol{u}(\boldsymbol{x},t) = \left\{u_\infty + \sin(x_1 - u_\infty t)\cos(x_2)e^{\frac{-2t}{Re}}, -\cos(x_1 - u_\infty t)\sin(x_2)e^{\frac{-2t}{Re}}\right\}$$

Here, the length and velocity scales used to define the Reynolds number are the same as that used in the previous stationary

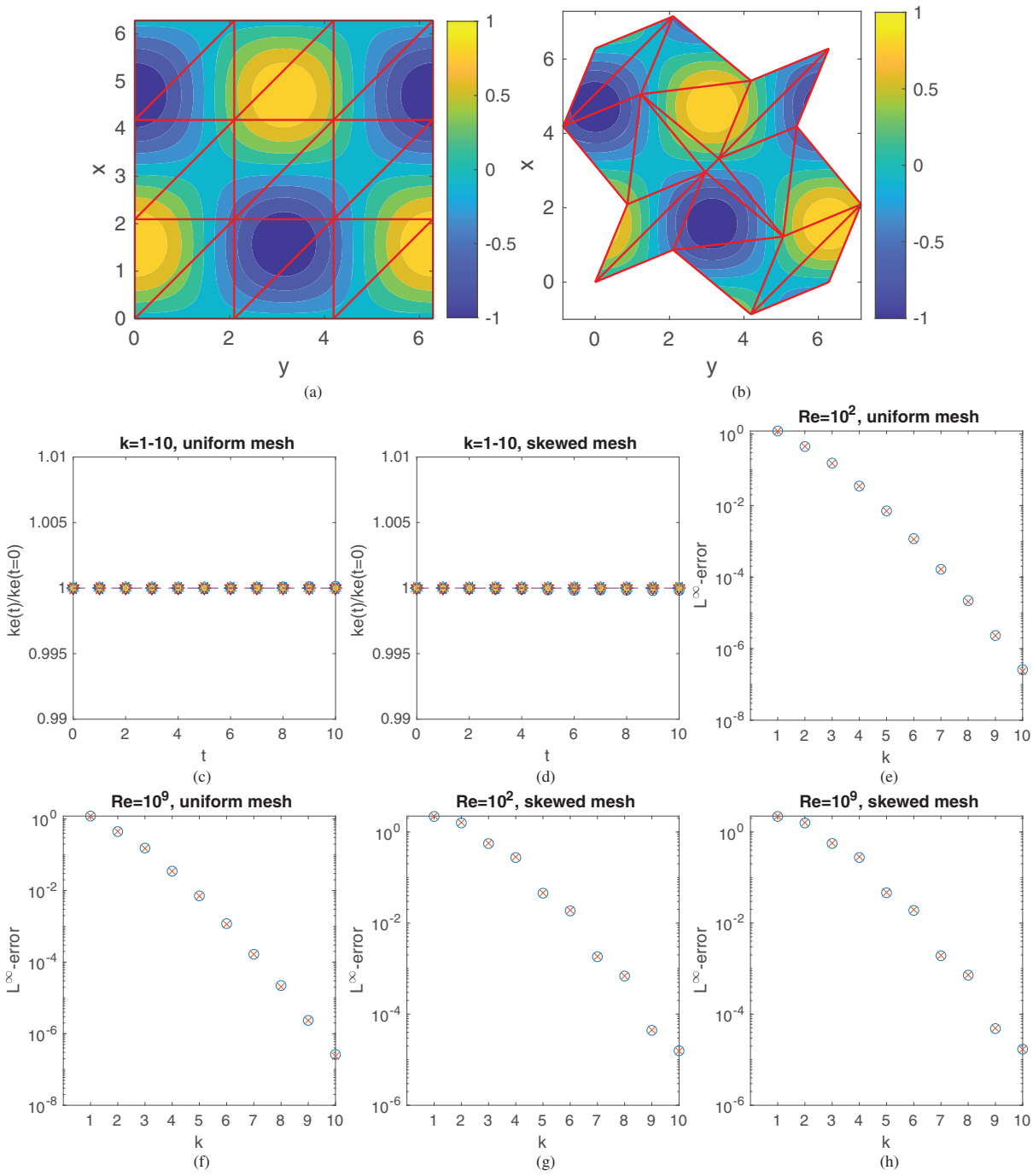

FIGURE 1 | Taylor–Green problem on a uniform and skewed mesh. (a) Uniform and (b) skewed 6×6 triangular mesh. Kinetic energy as a function of time (symbols – simulation, line – analytical) at Reynolds number 10^9 on the (c) uniform and (d) skewed mesh. Maximum absolute error as a function of polynomial degree for: (e) Reynolds number 10^2, uniform mesh, (f) Reynolds number 10^9, uniform mesh, (g) Reynolds number 10^2, skewed mesh, and (h) Reynolds number 10^9, skewed mesh. In (e–h), circle – u_1, and cross – u_2. [Colour figure can be viewed at wileyonlinelibrary.com]

Taylor–Green test case. u_∞ is the convective velocity and Re is the Reynolds number. We choose $u_\infty = 1$ and $Re = 10^9$. In the interest of brevity, we simulate this problem only for the skewed mesh (shown in Figure 1b) and only show convergence with p–refinement.

The velocity is computed at time $t = 1$ for degrees 1 to 10. Timestep used is 10^{-3}. Figure 3a,b show the computed velocity (x_1-component) for degree 10 and the discrete L^∞-error for the different degrees, respectively. The error, as expected, decays exponentially and is accurate up to four significant digits for degree 10.

7.3 | Lid-Driven Cavity

Next, we simulate an internal flow. We consider the lid-driven cavity problem at a Reynolds number of 5000. Figure 4a shows the unstructured mesh used. We use polynomial degree 5 to compute the solution. A Dirichlet boundary condition of $\boldsymbol{u} = (1, 0)$ is used

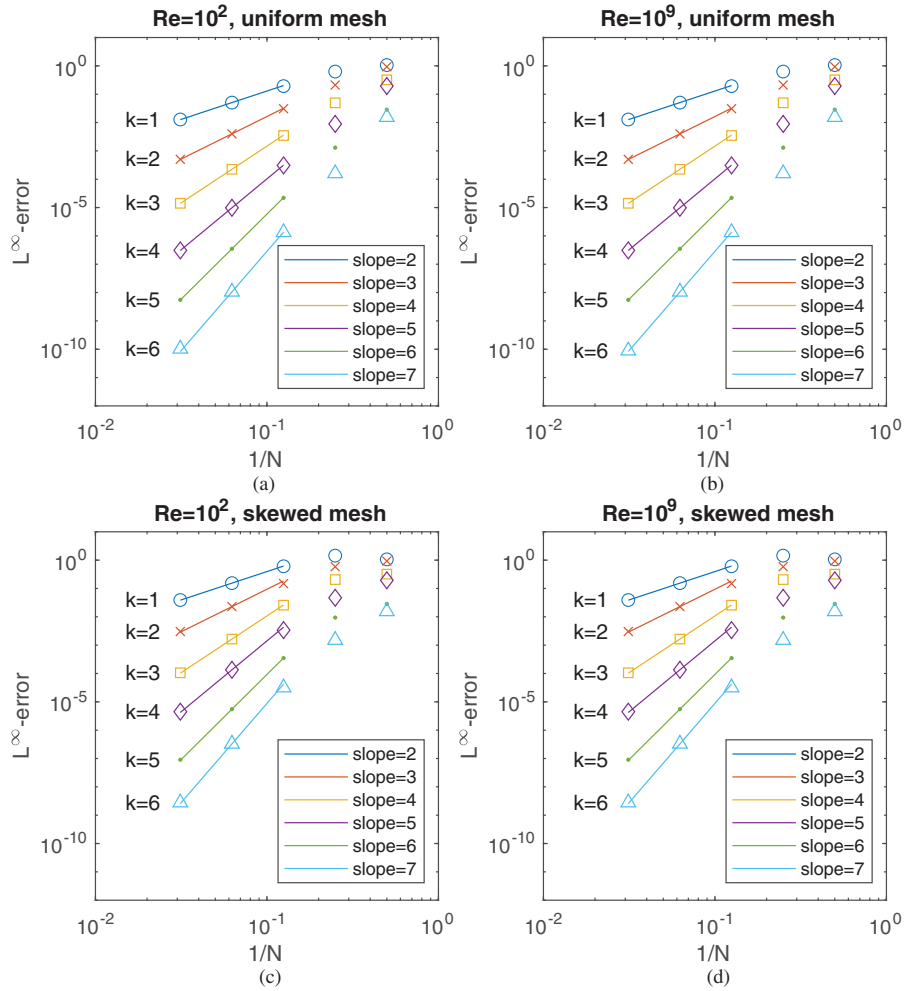

FIGURE 2 | Convergence for the Taylor–Green problem with mesh refinement. (a) $Re = 10^2$, uniform mesh. (b) $Re = 10^9$, uniform mesh. (c) $Re = 10^2$, skewed mesh. (d) $Re = 10^9$, skewed mesh. [Colour figure can be viewed at wileyonlinelibrary.com]

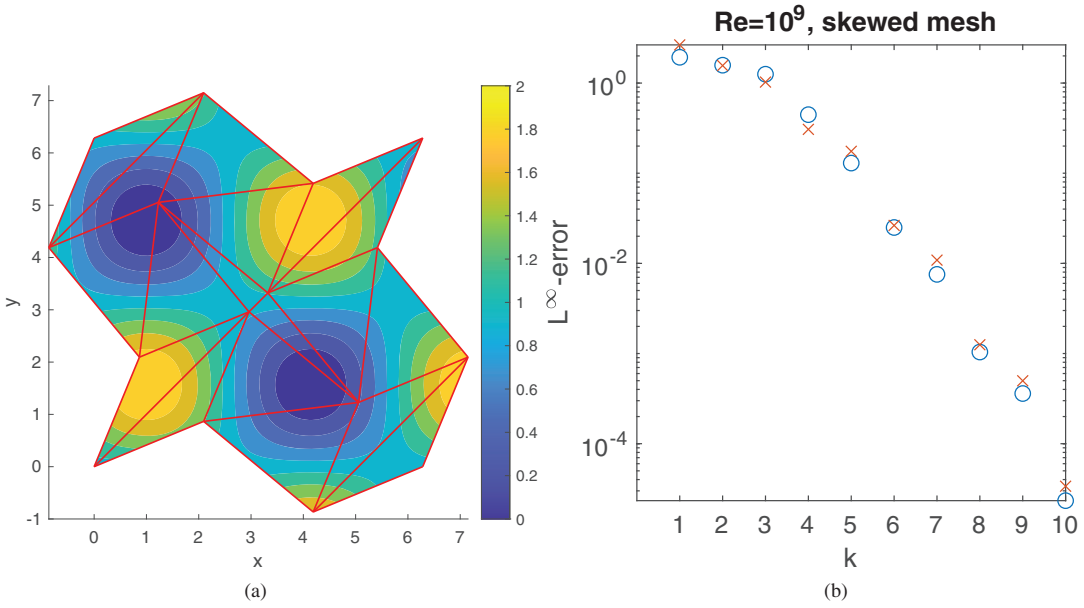

FIGURE 3 | Convecting Taylor–Green vortex at $Re = 10^9$. (a) x_1-component of the velocity at time $t = 1$ computed with degree 10. (b) L^∞-error of the computed velocity at time $t = 1$ as a function of polynomial degree (circle-u_1, cross-u_2). [Colour figure can be viewed at wileyonlinelibrary.com]

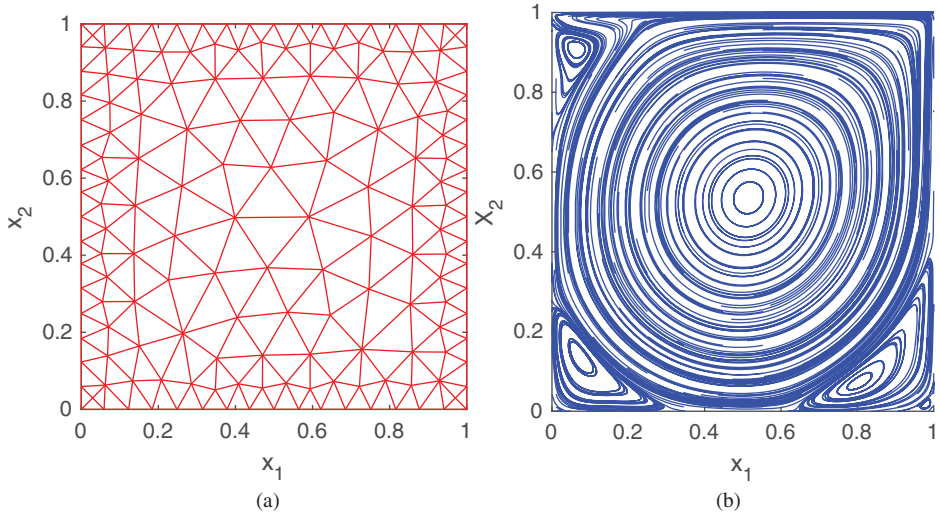

FIGURE 4 | Lid-driven cavity at a Reynolds number of 5000. (a) Mesh. (b) Streamlines of the steady state solution. [Colour figure can be viewed at wileyonlinelibrary.com]

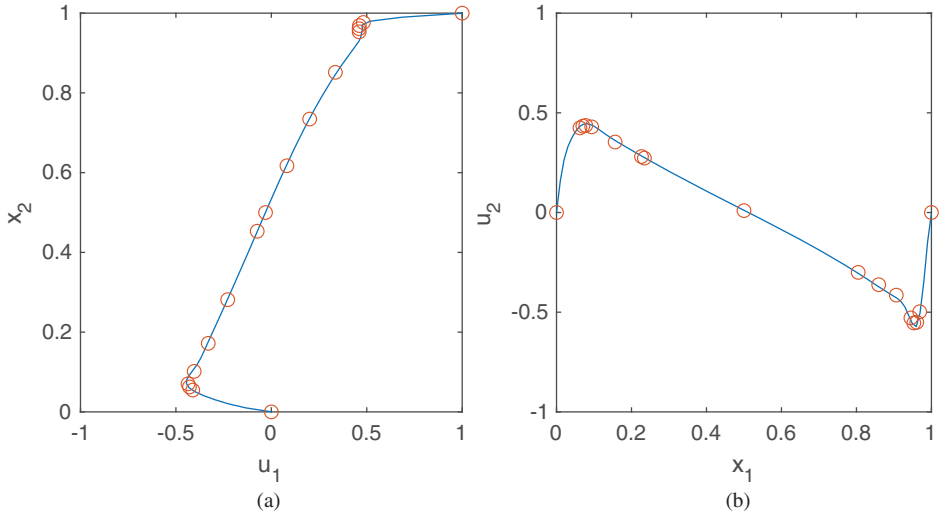

FIGURE 5 | Comparison of the steady-state lid-driven cavity results to [32] at Reynolds number 5000. (a) x_1-component versus x_2 at $x_1 = 0.5$. (b) x_2-component versus x_1 at $x_2 = 0.5$. Line–our simulation, symbol–[32]. [Colour figure can be viewed at wileyonlinelibrary.com]

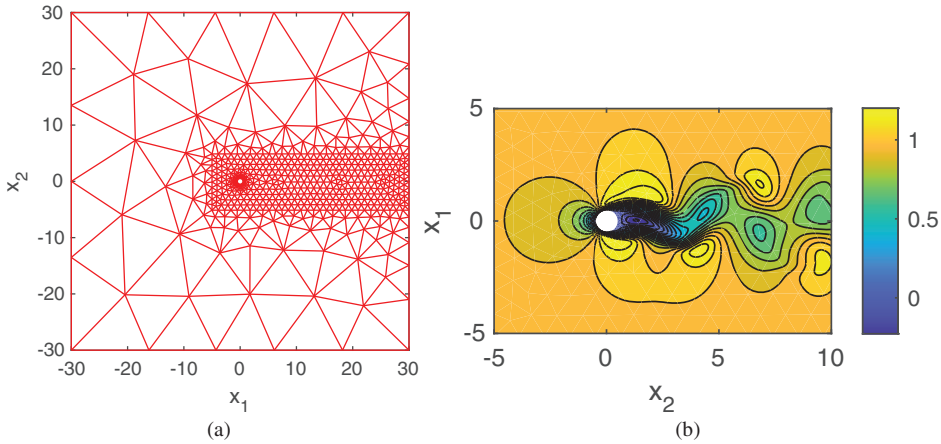

FIGURE 6 | Flow over a circular cylinder at a Reynolds number of 100. (a) Mesh. (b) Instantaneous flow. Contours show x_1-component of velocity. [Colour figure can be viewed at wileyonlinelibrary.com]

for the top wall and $\boldsymbol{u} = (0, 0)$ for the remaining walls. The streamlines of the computed steady state flow are shown in Figure 4b. For validation, we compare our steady state results to the simulation of [32]. The profiles of x_1-component of velocity along the centerline $x_1 = 0.5$ are compared in Figure 5a; good agreement is observed. Also, profile of the x_2-component of velocity along the centerline $x_2 = 0.5$ is compared in Figure 5b. They also agree well with the reference results.

7.4 | Flow Over a Circular Cylinder

Next, we simulate an external flow over a circular cylinder at a Reynolds number (UD/ν) of 100. Here, the velocity scale U is the freestream velocity. The length scale D is the diameter of the cylinder. ν is the kinematic viscosity. The mesh considered is shown in Figure 6a. A total of 1200 elements are used and a polynomial degree of 5 is used in each element of the mesh. All spatial coordinates are non-dimensionalized using the cylinder diameter D. The center of the cylinder is placed at $(0, 0)$. Its radius is 0.5. A large computational domain of $[-30, 30]^2$ is used to minimize the effect of boundary conditions on the vortex shedding. The mesh is refined close to the cylinder surface and also in a box of height 10 around the cylinder. All velocities are non-dimensionalized using the freestream velocity U. A Dirichlet boundary condition of $\boldsymbol{u} = (1, 0)$ is used on the left boundary. On the cylinder surface, a no-slip Dirichlet boundary condition of $\boldsymbol{u} = (0, 0)$ is used. On the top, bottom, and right boundaries, a zero freestream pressure is imposed by setting $(\nu \boldsymbol{L} - p\boldsymbol{I})\boldsymbol{n}$ to zero.

Figure 6b shows an instantaneous visualization of the simulated flow. The contours are of the x_1-component of velocity. The Von Karman vortex street is clearly visible in the wake of the cylinder. The x_2-component of velocity at a point $(1, 0)$ in the wake of the cylinder is shown in Figure 7 as a function of time. The Strouhal frequency extracted from this plot is 0.1647. It agrees well with the reference value of 0.164 of [33].

7.5 | Flow Over a Cylinder With Spikes

We simulate the flow over a complex geometry of a cylinder with spikes. The geometry of the spiked cylinder is shown in Figure 8a. The same large computational domain of $[-30, 30]^2$ that was used in the previous section is used for this problem. A total of 10 spikes are implanted on the cylinder. The coordinates of the nodes of the right-most spike are $(0.5\cos(\theta), 0.5\sin(\theta))$, $(0.5\cos(\theta), -0.5\sin(\theta))$, and $(0.5(\cos(\theta) + \sqrt{3}\sin(\theta), 0)$. The remaining spikes are the rotations of this spike at angular intervals $2\pi/10$.

An unstructured mesh for this geometry is carefully constructed by refining near the spikes and the walls of the cylinder. The near-wall mesh in the subdomain $[-1, 2] \times [-1, 1]$ is shown in Figure 8b. This fine near-wall mesh is coarsened through the subdomain $[-5, 30] \times [-5, 5]$. This subdomain mesh is shown in Figure 9. The overall computational mesh is shown in Figure 10.

A total of 1862 elements are used and a polynomial degree of five is used in each element. The velocity scale, length scale, and Reynolds number are the same as that used in the smooth cylinder case. A timestep of 2×10^{-3} is used for the simulation. The boundary conditions are the same as that of the smooth cylinder simulation.

Figure 11 shows an instantaneous snapshot of the vortex shedding behind the spiked cylinder. The near-wall x_1- and

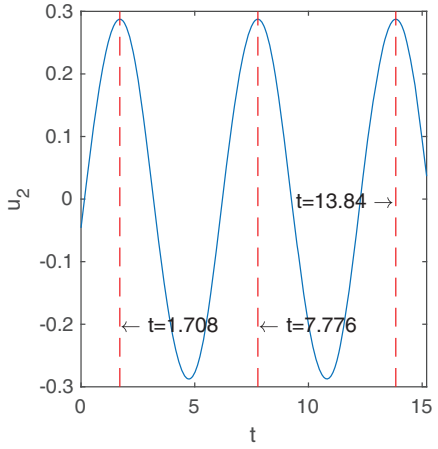

FIGURE 7 | Velocity at point $(1, 0)$ in the wake of the cylinder as a function of time. [Colour figure can be viewed at wileyonlinelibrary.com]

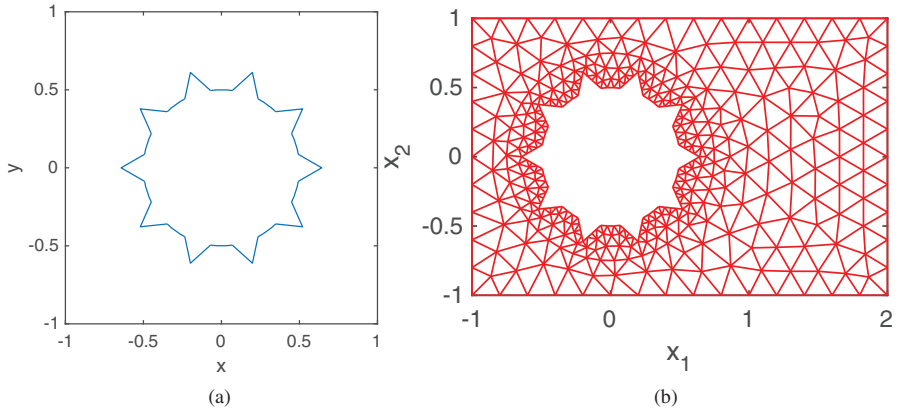

FIGURE 8 | (a) Geometry of the spiked cylinder. (b) Near-wall mesh in the subdomain $[-1, 2] \times [-1, 1]$ for the spiked cylinder. [Colour figure can be viewed at wileyonlinelibrary.com]

x_2-components are shown in Figure 12a,b, respectively. The x_2-component of the velocity at a point $(1, 0)$ in the wake of the cylinder is shown in Figure 13. The Strouhal number computed from this plot is 0.14 which is smaller than that for the smooth cylinder.

All the above numerical experiments were in 2D. Below we present some numerical experiments that demonstrate the features of our method in 3D.

7.6 | Taylor–Green Problem on a 3D Tetrahedral Mesh

The same Taylor–Green problem (Equation (71)) is solved in 3D on a tetrahedral mesh. The length and velocity scales are the same as that used for the 2D stationary Taylor–Green vortex. The mesh is shown in Figure 14a. It consists of 116 tetrahedral elements.

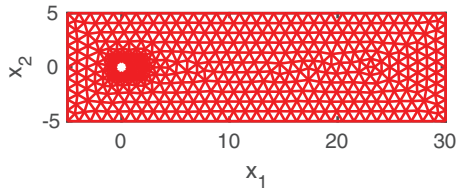

FIGURE 9 | Mesh in the subdomain $[-5, 30] \times [-5, 5]$. [Colour figure can be viewed at wileyonlinelibrary.com]

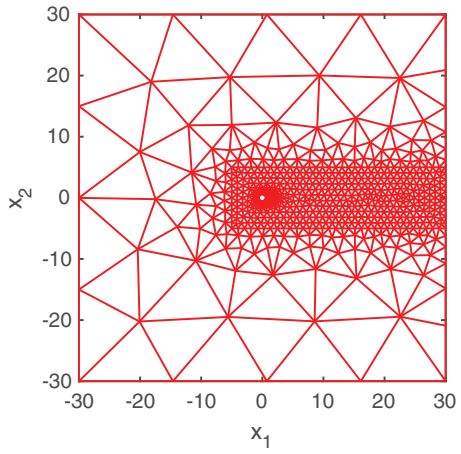

FIGURE 10 | Overall mesh in the full computational domain $[-30, 30]^2$. [Colour figure can be viewed at wileyonlinelibrary.com]

Periodic boundary conditions are used for the velocities. The triangular faces on the domain boundaries are carefully constructed such they are also periodic. This construction ensures that the mesh is consistent with the periodic boundary conditions.

7.6.1 | Non-Dissipative and Stable at High Reynolds Numbers

To show that our method is non-dissipative and stable at high Reynolds numbers, we simulate this problem at a high Reynolds number of 10^9 until time $t = 10$. Polynomial degrees considered are one to five. The evolution of kinetic energy with time is shown in Figure 14b. The exact kinetic energy is also plotted in the figure. Since the Reynolds number is high, the analytical kinetic energy remains close to the initial kinetic energy for a long time, that is, the kinetic energy does not dissipate much. This non-dissipative behavior is reproduced by our numerical solutions. Therefore, our method is non-dissipative in 3D. Furthermore, the kinetic energy remains bounded for all the degrees. This boundedness shows that our non-dissipative method is stable at high Reynolds numbers in 3D. The solution obtained with degree five at time $t = 1$ is shown in Figure 14c.

7.6.2 | Arbitrary Order Accuracy

In the interest of brevity, we show convergence only for p-refinement at a high Reynolds number of 10^9. Polynomial degrees considered are two to ten. We simulate the problem using a small timestep of 10^{-6} and for just ten timesteps. The discrete L^∞ error at the end of the tenth timestep is shown in Figure 14d.

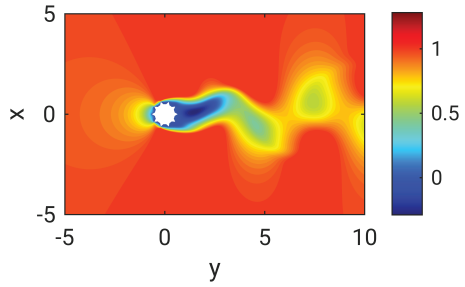

FIGURE 11 | Instantaneous visualization of flow around the cylinder with spikes. Contours of x_1-component of velocity. [Colour figure can be viewed at wileyonlinelibrary.com]

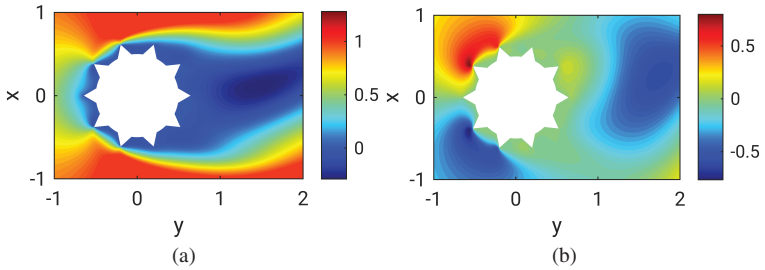

FIGURE 12 | Near-wall instantaneous visualization of flow around the cylinder with spikes. (a) x_1-component. (b) x_2-component. [Colour figure can be viewed at wileyonlinelibrary.com]

The discrete error is computed by evaluating the error at 800 uniformly spread points in each element and taking the maximum over all elements. Using a small timestep and a small number of timesteps isolates just the spatial discretization error. The error decays exponentially with the polynomial degree. The numerical solution is accurate up to five significant digits for degree five. This shows the arbitrary order accuracy of the method.

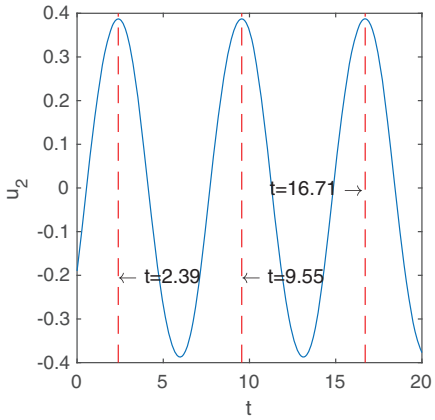

FIGURE 13 | Velocity at point $(1, 0)$ in the wake of the spiked cylinder as a function of time. [Colour figure can be viewed at wileyonlinelibrary.com]

7.7 | Homogeneous Isotropic Turbulence Problem on a 3D Tetrahedral Mesh

Finally, we demonstrate that our non-dissipative method remains stable when simulating a high Reynolds number turbulent flow on a coarse mesh without any subgrid model. We demonstrate this using the homogeneous isotropic turbulence problem. This demonstration is important because it shows that our method can be used as a base method to build a robust and accurate high-order large-eddy simulation methodology. We use the coarse mesh shown in Figure 14a. Reynolds numbers considered are 10^9, 10^6, 10^4, 10^3, and 10^2. The length and velocity scales are $1/2\pi \times$ (the box size) and the initial turbulence intensity, respectively. We use a polynomial degree of five and a timestep of 10^{-3}, for all the cases. The exact initial velocity field $\boldsymbol{u}(\boldsymbol{x}, t = 0)$ is prescribed using the procedure of [34] with parameters $\sigma = 4$, $k_p = 3$, and $q^2 = 3$. 32 wavenumbers are used along each direction to prescribe the exact initial velocity field.

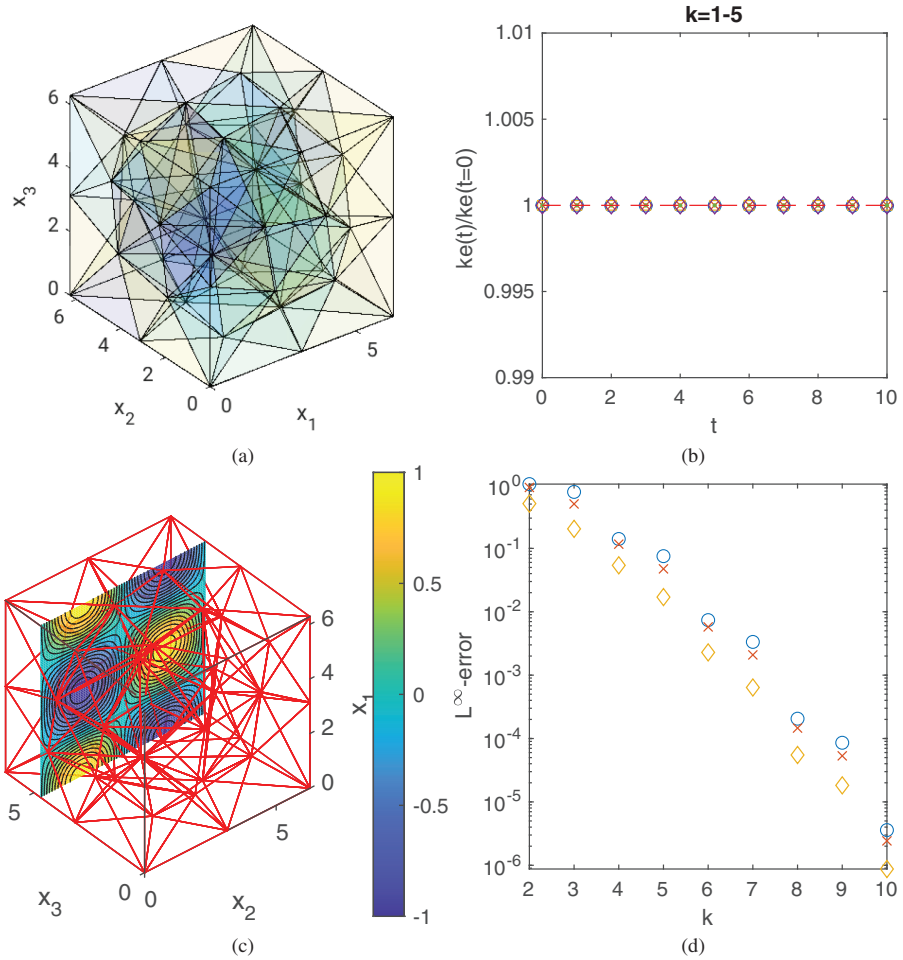

FIGURE 14 | Taylor–Green problem on a 3D tetrahedral mesh. (a) Mesh. (b) Kinetic energy versus time (symbols–numerical solution for degrees one to five, line–analytical). (c) Velocity (x_1-component) at time $t = 10$ for degree ten at $x_3 = 3\pi/2$. (d) Error versus polynomial degree. [Colour figure can be viewed at wileyonlinelibrary.com]

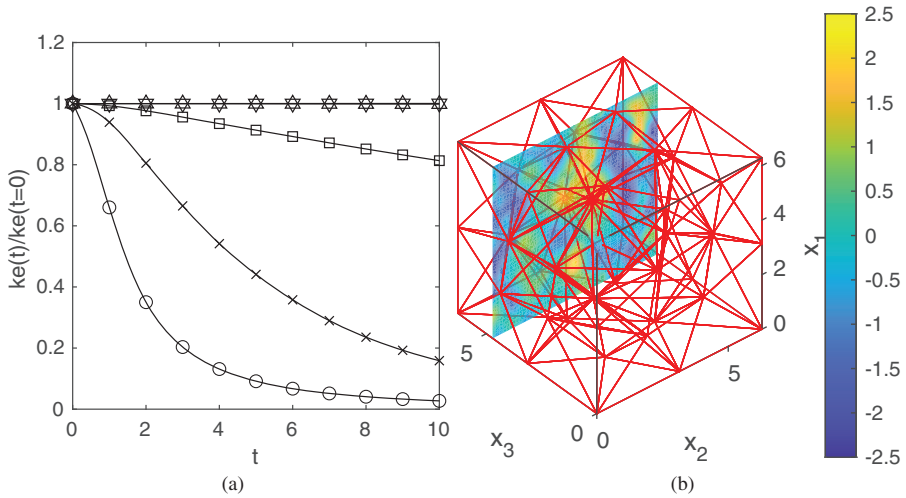

FIGURE 15 | Homogeneous isotropic turbulence problem on a 3D tetrahedral mesh. (a) Kinetic energy versus time, ∘: $Re = 10^2$, ×: $Re = 10^3$, □: $Re = 10^4$, △: $Re = 10^6$, and ▽: $Re = 10^9$. (b) Instantaneous velocity at time $t = 1$ at $Re = 10^2$. [Colour figure can be viewed at wileyonlinelibrary.com]

We time integrate the numerical solution until time $t = 10$. The evolution of numerical kinetic energy with time is shown in Figure 15a. The energy decays faster with increasing Reynolds number. The energy barely decays for the high Reynolds numbers $Re = 10^6$ and $Re = 10^9$ but remains bounded. This very small decay of energy is because at these high Reynolds numbers the length scale of turbulent dissipation (Kolmogorov scale) is not resolved by the coarse mesh. The boundedness of energy demonstrates the robustness of our method in such scenarios. An instantaneous visualization at time $t = 1$ for $Re = 10^2$ is shown in Figure 15b (polynomial degree used for this visualization is seven).

8 | Summary

In summary, for complex geometries, non-dissipative and energy-conserving numerical methods have been traditionally developed using the finite volume framework and they have been at best second-order accurate. This paper proposes an HDG method that is *non-dissipative, energy-conserving, and arbitrary high-order* accurate on unstructured triangular/tetrahedral meshes. An efficient implementation of the method using orthonormal and degree-ordered basis functions is also given. Results from numerical experiments demonstrating the different features of the method are also given.

To the best of our knowledge, this numerical method is the first non-dissipative and energy-conserving method that is arbitrary high-order accurate for incompressible flow simulations in complex geometries. Our presentation of the proposed HDG method is such that it is easy to access for finite-volume CFD engineers. The features of this HDG method make it an ideal base method for developing high-order LES techniques for incompressible flow simulations of complex geometries.

Acknowledgments

We acknowledge support from the United States Office of Naval Research under grants N00014-21-1-2454. We are thankful to Professor Bernardo Cockburn for useful discussions.

Data Availability Statement

Data sharing is not applicable to this article as no datasets were generated or analyzed during the current study.

References

1. R. Mittal and P. Moin, "Suitability of Upwind-Biased Finite Difference Schemes for Large-Eddy Simulation of Turbulent Flows," *AIAA Journal* 35, no. 8 (1997): 1415–1417.

2. B. Perot, "Conservation Properties of Unstructured Staggered Mesh Schemes," *Journal of Computational Physics* 159, no. 1 (2000): 58–89.

3. X. Zhang, D. Schmidt, and B. Perot, "Accuracy and Conservation Properties of a Three-Dimensional Unstructured Staggered Mesh Scheme for Fluid Dynamics," *Journal of Computational Physics* 175, no. 2 (2002): 764–791.

4. K. Mahesh, G. Constantinescu, and P. Moin, "A Numerical Method for Large-Eddy Simulation in Complex Geometries," *Journal of Computational Physics* 197, no. 1 (2004): 215–240.

5. F. Ham, K. Mattsson, G. Iaccarino, and P. Moin, "Towards Time-Stable and Accurate LES on Unstructured Grids," in *Complex Effects in Large Eddy Simulations* (Berlin Heidelberg: Springer, 2007), 235–249.

6. F. Trias, O. Lehmkuhl, A. Oliva, C. Pérez-Segarra, and R. Verstappen, "Symmetry-Preserving Discretization of Navier–Stokes Equations on Collocated Unstructured Grids," *Journal of Computational Physics* 258 (2014): 246–267.

7. B. Perot, "Discrete Conservation Properties of Unstructured Mesh Schemes," *Annual Review of Fluid Mechanics* 43, no. 1 (2011): 299–318.

8. M. O. Deville, P. F. Fischer, and E. H. Mund, *High-Order Methods for Incompressible Fluid Flow* (Cambridge: Cambridge university press, 2002).

9. L. Scott and M. Vogelius, "*Norm Estimates for a Maximal Right Inverse of the Divergence Operator in Spaces of Piecewise Polynomials*, ESAIM," *Mathematical Modelling and Numerical Analysis* 19, no. 1 (1985): 111–143.

10. P. Raviart and J. Thomas, "A Mixed Finite Element Method for Second Order Elliptic Problems," in *Mathematical Aspects of Finite Element Methods* (Berlin Heidelberg: Springer, 1975), 292–315.

11. F. Brezzi, J. Douglas, and D. Marini, "Two Families of Mixed Finite Elements for Second Order Elliptic Problems," *Numerische Mathematik* 47, no. 2 (1985): 217–235.

12. B. Cockburn and G. Fu, "Superconvergence by M-Decompositions. Part II: Construction of Two-Dimensional Finite Elements," *ESAIM. Mathematical Modelling and Numerical Analysis* 51, no. 1 (2017): 165–186.

13. B. Cockburn and G. Fu, "Superconvergence by M-Decompositions. Part III: Construction of Three-Dimensional Finite Elements," *ESAIM. Mathematical Modelling and Numerical Analysis* 51, no. 1 (2017): 365–398.

14. B. Cockburn, G. Fu, and F. Sayas, "Superconvergence by M-Decompositions. Part I: General Theory for HDG Methods for Diffusion," *Mathematics of Computation* 86, no. 306 (2017): 1609–1641.

15. B. Cockburn, G. Kanschat, and D. Schötzau, "A Locally Conservative LDG Method for the Incompressible Navier-Stokes Equations," *Mathematics of Computation* 74, no. 251 (2005): 1067–1095.

16. R. Temam, "Sur l'approximation de la solution des équations de navier-stokes par la méthode des pas fractionnaires (ii)," *Archive for Rational Mechanics and Analysis* 33 (1969): 377–385.

17. S. Charnyi, T. Heister, M. A. Olshanskii, and L. Rebholz, "On Conservation Laws of Navier–Stokes Galerkin Discretizations," *Journal of Computational Physics* 337 (2017): 289–308.

18. O. Lehmkuhl, G. Houzeaux, H. Owen, G. Chrysokentis, and I. Rodríguez, "A Low-Dissipation Finite Element Scheme for Scale Resolving Simulations of Turbulent Flows," *Journal of Computational Physics* 390 (2019): 51–65.

19. K. Goc, O. Lehmkuhl, G. Park, S. Bose, and P. Moin, "Large Eddy Simulation of Aircraft at Affordable Cost: A Milestone in Computational Fluid Dynamics," *Flow* 1 (2021): E14.

20. J. Guzmán and L. Scott, "The Scott-Vogelius Finite Elements Revisited," *Mathematics of Computation* 88, no. 316 (2019): 515–529.

21. P. Farrell, L. Mitchell, L. Scott, and F. Wechsung, "A Reynolds-Robust Preconditioner for the Scott-Vogelius Discretization of the Stationary Incompressible Navier-Stokes Equations," *SMAI Journal of Computational Mathematics* 7 (2021): 75–96.

22. M. Olshanskii and L. Rebholz, "Longer Time Accuracy for Incompressible Navier–Stokes Simulations With the EMAC Formulation," *Computer Methods in Applied Mechanics and Engineering* 372 (2020): 113369.

23. J. Guzmán, C. Shu, and F. Sequeira, "H(div) Conforming and DG Methods for Incompressible Euler's Equations," *IMA Journal of Numerical Analysis* 37, no. 4 (2017): 1733–1771.

24. C. Lehrenfeld and J. Schöberl, "High Order Exactly Divergence-Free Hybrid Discontinuous Galerkin Methods for Unsteady Incompressible Flows," *Computer Methods in Applied Mechanics and Engineering* 307 (2016): 339–361.

25. B. Cockburn, G. Kanschat, and D. Schötzau, "A Note on Discontinuous Galerkin Divergence-Free Solutions of the Navier–Stokes Equations," *Journal of Scientific Computing* 31 (2007): 61–73.

26. B. Cockburn and J. Gopalakrishnan, "Incompressible Finite Elements via Hybridization. Part I: The Stokes System in Two Space Dimensions," *SIAM Journal on Numerical Analysis* 43, no. 4 (2005): 1627–1650.

27. B. Cockburn and J. Gopalakrishnan, "Incompressible Finite Elements via Hybridization. Part II: The Stokes System in Three Space Dimensions," *SIAM Journal on Numerical Analysis* 43, no. 4 (2005): 1651–1672.

28. J. Carrero, B. Cockburn, and D. Schötzau, "Hybridized Globally Divergence-Free LDG Methods. Part I: The Stokes Problem," *Mathematics of Computation* 75, no. 254 (2006): 533–563.

29. B. Cockburn and F.-J. Sayas, "Divergence-Conforming HDG Methods for Stokes Flows," *Mathematics of Computation* 83, no. 288 (2014): 1571–1598.

30. G. Fu, Y. Jin, and W. Qiu, "Parameter-Free Superconvergent H(div)-conforming HDG Methods for the Brinkman Equations," *IMA Journal of Numerical Analysis* 39, no. 2 (2019): 957–982.

31. S. Anantharamu and K. Mahesh, "Arnoldi-Based Orthonormal and Hierarchical Divergence-Free Polynomial Basis and Its Applications," arXiv preprint, arXiv:2206.07889 (2022).

32. U. Ghia, K. Ghia, and C. Shin, "High-Re Solutions for Incompressible Flow Using the Navier-Stokes Equations and a Multigrid Method," *Journal of Computational Physics* 48, no. 3 (1982): 387–411.

33. A. Kravchenko, P. Moin, and K. Shariff, "B-Spline Method and Zonal Grids for Simulations of Complex Turbulent Flows," *Journal of Computational Physics* 151, no. 2 (1999): 757–789.

34. N. Mansour and A. Wray, "Decay of Isotropic Turbulence at Low Reynolds Number," *Physics of Fluids* 6, no. 2 (1994): 808–814.